

UNIVERSITY OF HAWAII LIBRARY

EVALUATION OF A COASTAL OCEAN MODEL FOR
OAHU, HAWAII

A THESIS SUBMITTED TO THE GRADUATE DIVISION OF THE UNIVERSITY
OF HAWAII IN PARTIAL FULFILLMENT OF THE REQUIREMENTS FOR THE
DEGREE OF
MASTER OF SCIENCE

IN

OCEAN AND RESOURCES ENGINEERING

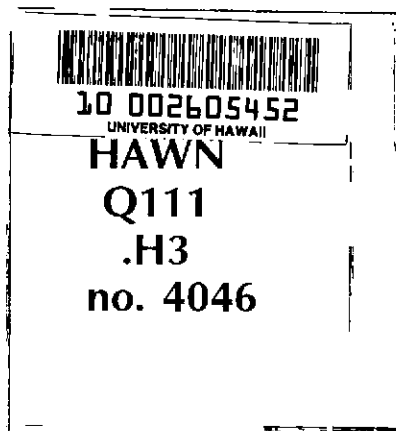
DECEMBER 2005

By


Andrew J. Wycklendt

Thesis Committee:
Kwok Fai Cheung, Chairperson
Geno Pawlak
Song K. Choi

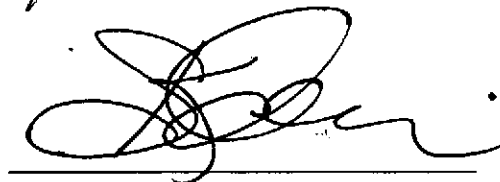
We certify that we have read this thesis and that, in our opinion, it is satisfactory in scope and quality as a thesis for the degree of Master of Science in Ocean and Resources Engineering.



THESIS COMMITTEE


Chairperson





Acknowledgements

First of all, I would like to thank God for making this all possible and providing the necessary resources to bring this study to a successful completion.

Special thanks goes to Project ENDEAVOR, Office of Naval Research grant number N00014-02-1-0903, for funding this research and the evaluations performed on the coastal ocean model ECOM, for without none of this could have been achieved.

I am especially grateful to Dr. Jim Lewis for letting me use his tuned model and for providing advice and support. Dr. Kwok Fai Cheung deserves acknowledgement for the invaluable guidance he has provided. I thank Dr. Geno Pawlak for helping me see the limitations of ocean modeling and its connections with oceanography. Dr. Song Choi deserves recognition for reviewing this thesis and adding insights from a different perspective. Additionally, I thank Ikaika Kincaid of Sea Engineering for providing the *field data and helping with its interpretation*.

I would also like to thank Edith Katada for reminding me of deadlines and making sure that they were met. Moreover, I would like to recognize Volker Roeber for taking time to view my results and listen to the conclusions I have formed, Alex Sanchez for the tips he provided regarding data filtering and presentation, Yong Wei for answering random questions about anything, and the rest of the Ocean and Resources Engineering Department and my family and friends for their advice and support.

Abstract

A coastal ocean model has been evaluated for Oahu, Hawaii. The three-dimensional hydrodynamic model used in this study is a semi-implicit version of ECOM that uses a z-level based coordinate system. The model has already been tuned and validated from the Eulerian viewpoint; however, it has not yet been validated from the Lagrangian perspective.

Sea level records as well as temperature and salinity profiles were first used to validate the tuning of this model. This validation was performed using statistical parameters, such as correlation coefficients and standard deviations, to quantitatively characterize the model's capabilities. The simulated current structure was then qualitatively compared with the known current structure of Mamala Bay. This qualitative comparison focused on the circulation trends experienced at the headlands and in the bay throughout a daily tide cycle.

After the model was successfully validated from the Eulerian perspective, its Lagrangian capabilities were then tested. The Lagrangian capabilities were tested by using the tuned model to virtually track drogues deployed on April 20, 2005 near the Sand Island outfall in Mamala Bay. The limited number of drogues deployed in this highly turbulent area restricted the ability to quantitatively analyze the Lagrangian results; therefore, these results were qualitatively analyzed to determine the model's Lagrangian capabilities. Successful validation of the model from both Eulerian and Lagrangian viewpoints demonstrate the "realism" of this coastal ocean model.

Table of Contents

Acknowledgements.....	iii
Abstract.....	iv
List of Tables	vii
List of Figures	viii
Chapter 1. Introduction	1
1.1 Background.....	1
1.2 Related Work	3
1.3 Objective.....	6
Chapter 2. Hawaii Regional Ocean Circulation.....	7
2.1 Hawaiian Archipelago Ocean Circulation	7
2.2 Mamala Bay Circulation.....	8
Chapter 3. The Ocean Circulation Model.....	14
3.1 Model Features.....	14
3.2 Governing Equations	15
3.3 Numerical Scheme.....	18
3.4 Initial and Boundary Conditions.....	18
Chapter 4. Field Measurements	24
4.1 The Experiment.....	24
4.2 The Results.....	25

Chapter 5. Model Evaluation	29
5.1 Model Preparation.....	29
5.2 Model Results	31
Chapter 6. Conclusions	45
Appendix A : APEC Location Data.....	48
Appendix B : APV Location Data	49
Appendix C : Curtain1 Location Data	50
Appendix D : Curtain2 Location Data	51
Appendix E : Eulerian Field Data Location Information.....	52
Appendix E: Field Cast Data Comparisons	53
Appendix F: Field Cast Statistics.....	59
Appendix G : Tidal Current Information	61
References.....	62

List of Tables

Table 1: Drifter Information	31
Table 2: Water Level Correlation and Average Error	33
Table 3 : Combined Field Cast Statistics	35
Table 4 : APEC Location Data	48
Table 5 : APV Location Data.....	49
Table 6 : Curtain1 Location Data.....	50
Table 7 : Curtain2 Location Data.....	51
Table 8 : Eulerian Field Data Location Information.....	52
Table 9 : Temperature Statistics	59
Table 10 : Salinity Statistics	59
Table 11 : Sound Speed Statistics.....	60
Table 12 : Tidal Current Locations.....	61
Table 13 : Tidal Current Ellipse Information with a 95% Confidence Interval	61

List of Figures

Figure 1: Coastal Currents around the Hawaiian Islands (Laevastu <i>et al.</i> , 1964)	8
Figure 2: Oahu's South Shore Offshore Disposal Sites (Torreson <i>et al.</i> , 1995)	10
Figure 3: M_2 Tidal Current Ellipses (Hamilton <i>et al.</i> , 1995).....	12
Figure 4: K_1 Tidal Current Ellipses (Hamilton <i>et al.</i> , 1995).....	12
Figure 5: Curtain1 [Blue] and Curtain2 [Red] Trajectories.....	25
Figure 6: APEC [Blue] and APV [Red] Horizontal Trajectories	26
Figure 7: APEC [Blue] and APV [Red] Vertical Trajectories.....	26
Figure 8: Honolulu Harbor Measured Water Level	27
Figure 9: Curvilinear Orthogonal Model Grid for Oahu, Hawaii	29
Figure 10 : Field Study Domain and Grid Spacing.....	30
Figure 11: Honolulu Harbor Tide Comparison.....	32
Figure 12 : Combined Field Cast Statistical Comparison.....	34
Figure 13 : Mamala Bay Current Structure.....	36
Figure 14 : Flood and Ebb Currents.....	38
Figure 15 : M_2 Tidal Current Ellipses	39
Figure 16 : Mamala Bay Density Structure Longitudinal Slice.....	40
Figure 17 : Virtual Particle Tracking Horizontal Scenarios	42
Figure 18 : Virtual Particle Tracking Vertical Scenarios.....	43
Figure 19 : Field Cast 1 Data Comparison.....	53
Figure 20 : Field Cast 2 Data Comparison.....	53

Figure 21 : Field Cast 3 Data Comparison.....	54
Figure 22 : Field Cast 4 Data Comparison.....	54
Figure 23 : Field Cast 5 Data Comparison.....	55
Figure 24 : Field Cast 6 Data Comparison.....	55
Figure 25 : Field Cast 7 Data Comparison.....	56
Figure 26 : Field Cast 8 Data Comparison.....	56
Figure 27 : Field Cast 9 Data Comparison.....	57
Figure 28 : Field Cast 10 Data Comparison.....	57
Figure 29 : Field Cast 11 Data Comparison.....	58
Figure 30 : Field Cast 12 Data Comparison.....	58

Chapter 1. Introduction

1.1 Background

According to Webster's dictionary, a model is defined as a simplified description of a complex entity or process. In engineering, a model is a human construct used to better understand real-world systems and processes. As a substitute for the real system, models are used when it is easier or more feasible to work with the substitute than with the actual system (Ford, 1999). Former aeronautical engineer and professor in the Department of Ocean Engineering at Florida Atlantic University, Dr. Jeffrey Tennant, often defined engineering as "the art of approximation". Engineers use many types of models to predict, analyze, and reconstruct processes that are often either impossible or too expensive to measure.

Various classes of models are used to "approximate" real-world system response. The various classifications of models include: conceptual, physical, mathematical, statistical, and visual (Ford, 1999).

- Conceptual models are qualitative models that help highlight important connections in real-world systems.
- Physical models are physical systems that can be easily observed and manipulated and which have characteristics similar to key features of more complex real-world systems.

- Mathematical models, including both analytical and numerical models, are developed by mathematically solving the relevant physics-based equations of a system to determine its behavior throughout time and space.
- Statistical models, although mathematical in nature, facilitate the characterization of a system based on statistical parameters and are useful in helping identify patterns and underlying relationships between data sets.
- Visualization models include anything that can help one visualize how a system works. A visualization model can be a direct link between data and some graphic or image output, or can be linked in series with some other type of model to convert its output into a visually useful format.

Although there are several model classes, a well developed model of a real-world system will often include aspects of each individual model class described above.

All previously defined model classes are used in this thesis to describe a real-world system. Conceptual modeling techniques are initially used to determine the appropriate mathematical model. A numerical physics-based mathematical model is then applied to simulate the real-world system. Coupled with the numerical model, combined statistical and physical (assimilation) models are used to determine the appropriate initial and boundary conditions. Finally, visual models are employed to present the results of the model package and compare the “approximation” with real-world measurements.

1.1.1 Environmental Modeling

Environmental modeling encompasses the modeling of land, air, and sea interactions. In addition to traditional forecasting and hindcasting abilities, environmental models are also used to explain complex processes within the modeled environment. Essential in the design of both complicated and simple systems, environmental modeling provides the ability to determine the dynamic response of a system to real-world external forces (SNAME, 1989). Real-world environment models coupled with a model that accurately represents an engineered system, such as a ship or floating crane, often results in a high fidelity model of the system operating in the real-world. This coupled modeling approach is especially important in arenas where it is either difficult or impossible to test the response of an engineered system in its operating environment, such as underwater vehicles operating in the dynamic coastal environment (Brutzman, 1994). Therefore, it is essential that the ocean environment be accurately modeled to provide a “realistic” virtual environment to test newly designed or altered ocean systems.

1.2 Related Work

The exponential growth of computer power is rapidly launching the new field of computational science; multidisciplinary research teams are beginning to develop large-scale predictive simulations of highly complex technical problems (Post and Votta, 2005). As an example, today’s computational power has provided the opportunity to create several high fidelity ocean models. A brief list of commercial and government supported ocean models include: the Princeton Ocean Model (POM), WAVEWATCH III

(WW3), the Estuary and Coastal Ocean Model (ECOM), Simulating WAVes Nearshore (SWAN), and the Navy Coastal Ocean Model (NCOM). These high fidelity ocean circulation and wave propagation simulation packages are just a few examples of available 21st century real-world environment models.

1.2.1 The Princeton Ocean Model

Blumberg and Mellor (1987) developed the Princeton Ocean Model, hereafter referred to as POM, during late 1970's and early 1980's. Initially the model was developed and applied to oceanographic problems in the Atmospheric and Oceanic Sciences Program of Princeton University, the Geophysical Fluid Dynamics Laboratory of the National Oceanic and Atmospheric Administration (NOAA), and Dynalaysis of Princeton. Although POM initially was used as a research tool, its success has resulted in the formulation of various other global and coastal ocean models. POM's success is demonstrated by its widespread use in applications such as: research on ocean response to global warming and future climate change (Ezer, 2001); ocean basin circulation research (Ezer and Mellor, 1997); simulations of past climatic changes (Ezer, 1999); in addition to model and altimetry assimilation (Mellor and Ezer, 1991).

1.2.2 The Estuary and Coastal Ocean Model

POM has become well-known in the world of ocean modeling because confidence has been established that the predominant physics are realistically reproduced by the model. Building upon that success, modifications have been introduced to the model which emphasize the physical processes occurring in the shallower portions of the world's

oceans, namely the estuary and coastal ocean environment. The technical changes introduced to POM to form ECOM include (Blumberg, 1996):

- A semi-implicit method in which the barotropic pressure gradient in the momentum equations and the horizontal velocity divergence in the continuity equations are treated implicitly.
- An option to use a z-level based coordinate system containing a vertical coordinate which is discretized using horizontally-constant grid spacing.
- An ability to handle flooding and drying of tidal flat regions.
- A choice of numerical advection schemes for controlling numerical dispersion.
- A capability to simulate suspended sediment transport.

Additionally, ECOM has been enhanced to include surface wave models, better bottom shear stresses for bottom boundary layer physics, and dissolved and sediment-bound tracer capabilities. Although ECOM is relatively new when compared to POM, with its introduction in the late 1980's, the model's underlying physics, derived from the physics of POM, and its successful validation in various hydrodynamic studies has driven confidence in ECOM to that similar of POM. A brief list of successful ECOM applications include: numerical simulations of internal tides (Lewis *et al.*, 2001); analysis of harbor region hydrodynamics (Blumberg *et al.*, 1999); modeling of transport processes (Blumberg *et al.*, 1993); in addition to model and current data assimilation (Lewis *et al.*, 1998).

1.2.3 Modeling Hawaii's Ocean Circulation

Modeling ocean circulation in the Hawaiian waters has received increasing attention over the last decade as a result of the Mamala Bay Study and the Hawaii Ocean Mixing Experiment. The demands of these two significant projects, in addition to others, require an ocean prediction system for the Hawaiian Islands. To fulfill this requirement, Lewis *et al.* (2001) has tested and validated a three-dimensional version of ECOM around the island of Oahu. Moreover, studies have also been performed that focus on the interaction of Mamala Bay's complex current structure with the Sand Island sewage outfall plume (Roberts, 1999a; Roberts, 1999b; Connolly *et al.*, 1999).

1.3 Objective

The objective of this thesis is to evaluate the “realism” of a real-world coastal ocean model. In the past, coastal ocean models have been tuned and validated using sea level records, temperature and salinity data, in addition to Acoustic Doppler Current Profiler (ADCP) Eulerian current measurements. Although several particle tracking simulations using high fidelity coastal ocean models have been run, their validation has been limited (Tetra Tech, 2000). Therefore, the objective of this thesis, more accurately defined, is to evaluate the model's “realism” from the Lagrangian perspective. To accomplish this objective, the model calibrated by Lewis *et al.* (2001) will be used to virtually track drogues deployed near the Sand Island outfall on April 20, 2005 (Sea Engineering and OCEES, 2005). The model's results will then be compared with field measurements and observations to evaluate the “realism” of the coastal ocean model.

Chapter 2. Hawaii Regional Ocean Circulation

Circulation patterns experienced in the coastal waters around Hawaii are a result of the Islands' unique bathymetry and tropical location in the middle of the Pacific Ocean. The strong currents experienced at the headlands and in the deep narrow channels between the Islands are features common to many island chains. The stratified waters created by the intense heating of the ocean by the tropical sun are characteristics common to regions located in the tropics. Altogether, the slope and unique bathymetry of the Hawaiian Islands, as they extend from the ocean surface to the abyssal sea floor, combined with the stratified waters provide the environment necessary to generate internal waves. Therefore, the resulting barotropically forced internal waves are the source of the unique circulation patterns found in the coastal waters of the Hawaiian Islands.

2.1 Hawaiian Archipelago Ocean Circulation

Circulation patterns observed in the Hawaii region can be broken down into several components: baroclinic currents, tidal currents, wind-induced currents, and wave-induced currents (Gerritsen, 1978). Baroclinic currents are produced by horizontal density gradients. Tidal currents, on the other hand, are generated by the gravitational effects of the sun and the moon. Although weak in the greater depths of the open ocean, tidal currents become significant in shallow coastal areas and account for 60 to 90 percent of Hawaii's total current activity (St. Denis, 1974). The effect of wind on currents is different for deep and shallow waters. In deep water wind generated currents demonstrate themselves as the Ekman drift; however, in shallow water the direction of the wind-

material, pesticides, waste water, and other forms of pollution. Circulation studies of this locally impacted marine environment provide key information on the distribution and transport of possible contaminants. The two recent studies of Mamala Bay's circulation include the Mamala Bay Study and the Hawaii Ocean Mixing Experiment.

2.2.1 The Mamala Bay Study

In the past, the bathing beaches of Honolulu periodically experienced bacteria levels above state standards (Environment Hawaii, 1995). Figure 2 shows the location of three major waste disposal sites in Mamala Bay (the former Pearl Harbor site, the former Honolulu Harbor site, and the active south Oahu site), two U.S. Army Corps of Engineers study sites used as part of the process for designating the south Oahu site in 1980, and a 1972 disposal site. The offshore outfall discharges from two primary treatment plants were the suspected cause of the reported high bacteria levels and an investigation was funded to determine their contribution as well as that of urban agricultural runoff. As a result of this investigation, Connolly *et al.* (1999) identified two sources as primary contributors to contamination within Mamala Bay: the outfall from the Sand Island wastewater treatment plant and the Ala Wai Canal.

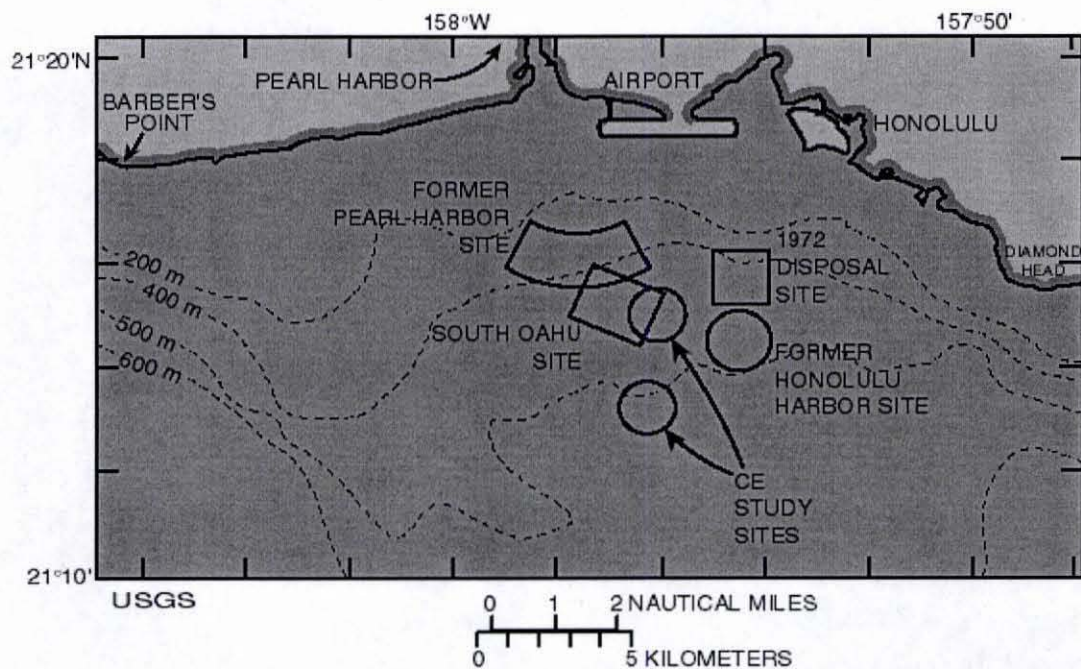


Figure 2: Oahu's South Shore Offshore Disposal Sites (Torreson *et al.*, 1995)

2.2.2 The Hawaii Ocean Mixing Experiment

The Hawaii Ocean Mixing Experiment, hereafter referred to as HOME, is a National Science Foundation (NSF) program to study tidally induced ocean mixing in the vicinity of the Hawaiian Ridge. The experiment is divided into five programs which include: historic data analysis, modeling, survey, in addition to far-field and near-field components. Data analysis and modeling objectives include the identification of locations along the ridge where barotropic-baroclinic conversion processes are strong and where mixing is likely to occur. Guided by this information, the survey and observational program is able to conduct high resolution site specific reconnaissance to better understand the energy transport and mixing processes. The two major goals of HOME are to isolate baroclinic variability associated with the tides from a background of

energetic processes and to extrapolate the results obtained from HOME to other regions of the ocean where tides are an important energy source for pelagic mixing (Luther *et al.*, 1999). HOME's efforts have resulted in the further gathering and analysis of data necessary to achieve HOME's goals and the development of ocean circulation models that include the effects of internal waves.

2.2.3 Observed Ocean Circulation

The oceanographic data relevant to this region are discussed and analyzed in detail by Hamilton *et al.* (1995). Major contributions to the currents, in both this area and throughout the Hawaiian Islands, come from tidal and low-frequency processes. The semidiurnal (M_2) tide approaches Oahu from the northeast. The wave splits east and west of the island, merges in Mamala Bay, and continues to propagate to the southwest. This results in strong currents at the headlands, Diamond Head and Barbers Point, which flow in practically opposite directions; the current amplitudes gradually reduce from approximately 25 cm/s at the headlands to zero near the midpoint between Pearl Harbor and Barbers Point (Figure 3). In contrast, the diurnal tides (K_1 and O_1) result in relatively uniform along-isobath flow in the bay (Figure 4). Therefore, the relative magnitudes of the currents that are due to both diurnal and semidiurnal tides vary throughout the bay. At the headlands the currents are mainly dominated by the semidiurnal tide. In the embayment the semidiurnal tide decreases resulting in tidal currents that are mainly diurnal.

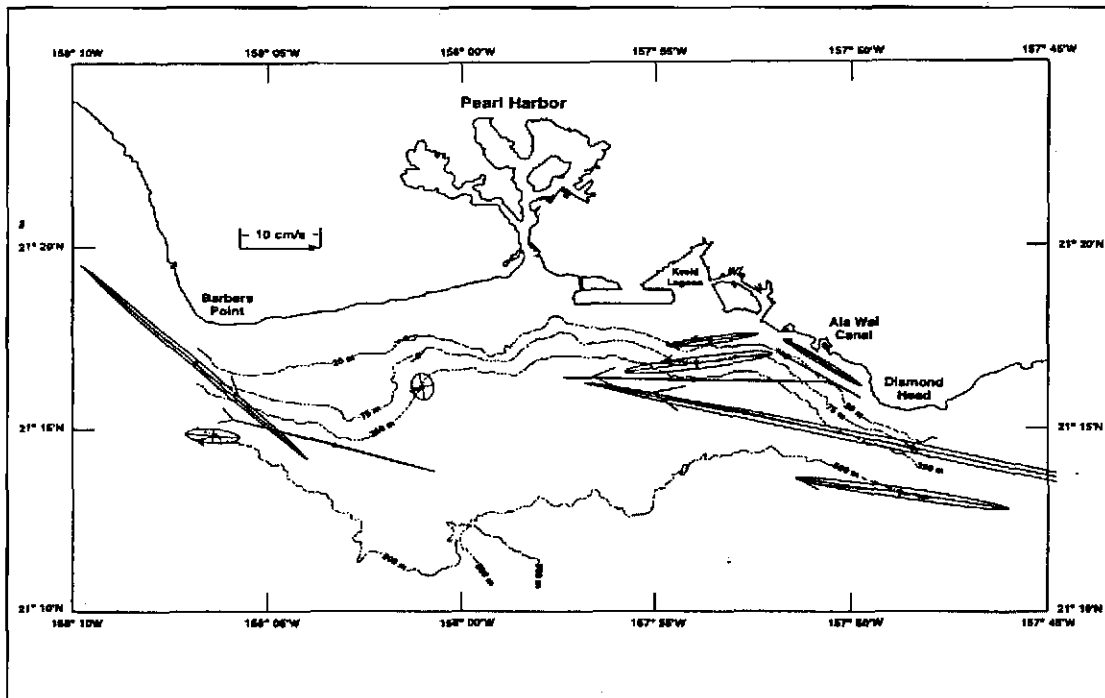


Figure 3: M₂ Tidal Current Ellipses (Hamilton *et al.*, 1995)

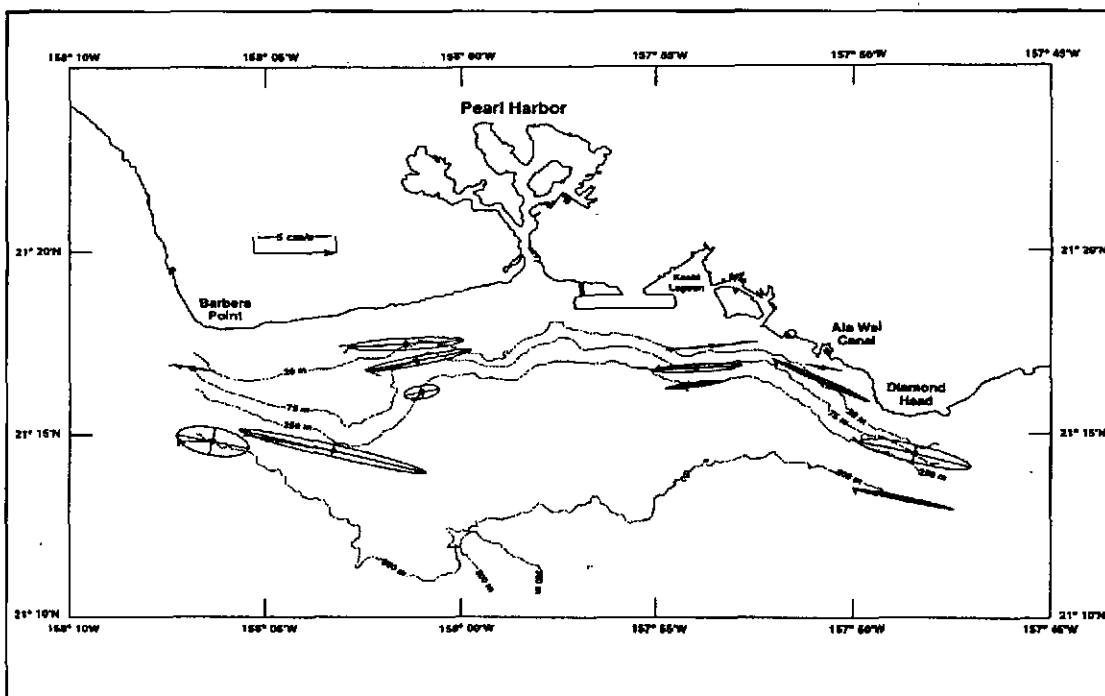


Figure 4: K₁ Tidal Current Ellipses (Hamilton *et al.*, 1995)

According to Hamilton *et al.* (1995), it is the interaction of the semidiurnal tide with the topography of Oahu that causes the large temperature fluctuations (internal waves) observed in this area. Eich *et al.* (2004) interpreted the opposing velocities at the headlands and the enhanced displacements near the bay center as a standing-wave pattern between non-locally generated eastward- and westward-propagating waves. As a result of these large vertical displacements, baroclinic currents and mixing processes are strong. Moreover, Alford *et al.* (2005) observed that the coherent processes in the eastern side of the bay lead those of the western side in phase, resulting in a western-propagating wave with a phase speed of about 1 m/s.

The subtidal current flows are also complex. These currents typically travel along isobaths with their amplitudes varying throughout the bay. A jet pattern, perhaps part of an offshore eddy approaching the coast, is the only explanation for their deeply penetrating flows (Hamilton *et al.*, 1995). Two distinct periods are observed. During the first half of the year, longer-period (10- to 20-day) motions tend to dominate and the mean flow pattern is directed out of the bay at Barbers Point and Diamond Head; daily average subtidal flows have been observed to exceed 60 cm/s. In summer, the mean flow generally reverses and shorter-period (1- to 5-day) fluctuations tend to dominate; daily average subtidal flows can reach magnitudes of 30 cm/s. Additionally, it appears that nearshore currents are more influenced by current fluctuations over the steep slope than by the local along-shore winds.

Chapter 3. The Ocean Circulation Model

3.1 Model Features

ECOM is a state-of-the-art hydrodynamic and sediment transport model which realistically computes water circulation, temperature and salinity, mixing, as well as transport, deposition and resuspension of cohesive and non-cohesive sediments (HydroQual, 2002). ECOM is based on the primitive equations of mass conservation, momentum balance, and turbulence closure. These governing equations accommodate the nonlinear advection of mass and momentum that is important in shallow water, turbulent mixing induced by both wind stress and bottom friction, baroclinic currents induced by horizontal density gradients, and barotropic currents produced by surface slopes.

The principal attributes of the model are as follows (Blumberg and Mellor, 1987):

- It addresses mesoscale phenomena, which is activity characterized by 1-100 km length and tidal-30 day time scales commonly observed in estuaries and the coastal ocean.
- The prognostic variables are the two components of velocity, temperature, salinity, and turbulent kinetic energy.
- Free surface elevation is also calculated prognostically with only some sacrifice in computational time so that tides and storm surge events can also be simulated.

- The prognostic equations governing the thermodynamic quantities account for water mass variations brought about by highly time-dependent coastal upwelling/downwelling processes as well as horizontal advective processes.
- It incorporates a turbulence closure model to provide a realistic parameterization of the vertical mixing processes.
- The momentum equations are nonlinear and incorporate a variable Coriolis parameter.
- It accommodates realistic coastline geometry and bottom topography.
- The horizontal grid can be defined with a curvilinear orthogonal coordinate system.

HydroQual (2002) provides a detailed description of ECOM in their software primer. Included below is a brief summary of the governing equations, numerical methods, in addition to the model's initial and boundary conditions.

3.2 Governing Equations

First, the coordinate system used in ECOM should be defined. ECOM uses a right handed coordinate system referenced to the Mean Sea Level (MSL) with the positive z-axis normal to and pointing out of the undisturbed water surface. Furthermore, it should also be noted that all times in the model are referenced to the Universal Time Zone (UTZ).

ECOM is based on the primitive equations of motion. The continuity equation can be written as:

$$\nabla \cdot \vec{V} + \frac{\partial w}{\partial z} = 0 \quad (1)$$

where \vec{V} is the two-dimensional velocity vector with components (u, v) and ∇ is the horizontal gradient operator. With ρ_0 as the reference density, ρ as the in-situ density, g the gravitational acceleration, P the pressure, K_M the vertical eddy diffusivity of turbulent mixing, and f as a latitudinal variation of the Coriolis parameter, the Reynolds-averaged momentum equations can be written as:

$$\frac{\partial u}{\partial t} + \vec{V} \cdot \nabla u + w \frac{\partial u}{\partial z} - fv = -\frac{1}{\rho_0} \frac{\partial P}{\partial x} + \frac{\partial}{\partial z} \left(K_M \frac{\partial u}{\partial z} \right) + F_x \quad (2)$$

$$\frac{\partial v}{\partial t} + \vec{V} \cdot \nabla v + w \frac{\partial v}{\partial z} - fu = -\frac{1}{\rho_0} \frac{\partial P}{\partial y} + \frac{\partial}{\partial z} \left(K_M \frac{\partial v}{\partial z} \right) + F_y \quad (3)$$

$$\rho g = -\frac{\partial P}{\partial z} \quad (4)$$

From the above equations, F_x and F_y are the horizontal mixing components in the x and y directions respectively. Derived from the Reynolds-averaged momentum equation in the vertical direction, the absolute pressure can be written as:

$$P(x, y, z, t) = P_{atm} + g \rho_0 \eta + g \int_z^0 \rho(x, y, z', t) dz' \quad (5)$$

where P_{atm} is the assumedly constant atmospheric pressure.

The conservation equations for temperature and salinity can be written as:

$$\frac{\partial \theta}{\partial t} + \vec{V} \cdot \Delta \theta + w \frac{\partial \theta}{\partial z} = \frac{\partial}{\partial z} \left[K_H \frac{\partial \theta}{\partial z} \right] + F_\theta \quad (6)$$

$$\frac{\partial S}{\partial t} + \vec{V} \cdot \Delta S + w \frac{\partial S}{\partial z} = \frac{\partial}{\partial z} \left[K_H \frac{\partial S}{\partial z} \right] + F_S \quad (7)$$

where θ is the potential temperature (or in-situ temperature for shallow water applications), S is the salinity, and K_H is the vertical eddy diffusivity for turbulent mixing for both heat and salt. Using temperature and salinity, the density is computed according to an equation of state of the form:

$$\rho = \rho(\theta, S) \quad (8)$$

given by Fofonoff (1962). All motions induced by small-scale processes not directly resolved by the model grid are parameterized in terms of horizontal mixing processes. These horizontal mixing processes are defined as:

$$F_x = \frac{\partial}{\partial x} \left[2A_M \frac{\partial u}{\partial x} \right] + \frac{\partial}{\partial y} \left[A_M \left(\frac{\partial u}{\partial y} + \frac{\partial v}{\partial x} \right) \right] \quad (9)$$

$$F_y = \frac{\partial}{\partial y} \left[2A_M \frac{\partial v}{\partial y} \right] + \frac{\partial}{\partial x} \left[A_M \left(\frac{\partial u}{\partial y} + \frac{\partial v}{\partial x} \right) \right] \quad (10)$$

$$F_{\theta,S} = \frac{\partial}{\partial x} \left[A_H \frac{\partial(\theta,S)}{\partial x} \right] + \frac{\partial}{\partial y} \left[A_H \frac{\partial(\theta,S)}{\partial y} \right] \quad (11)$$

where A_M and A_H are the horizontal diffusivities.

The vertical mixing is estimated using the Mellor and Yamada second-order turbulence closure with extensions from Galperin *et al.* (Mellor and Yamada, 1982; Galperin *et al.*, 1988); the extension prevents the mixing length from being overestimated in the stratified condition.

3.3 Numerical Scheme

ECOM uses a semi-implicit finite difference scheme, forward in time and centered in space, which eliminates the CFL condition for the propagation of tides required by the explicit finite difference scheme. The disadvantage of this numerical scheme is its numerical diffusivity and energy-dissipation which could over-damp free waves (Martin *et al.*, 1998). However, in this modeling case the motion of interest is predominantly forced by tides and low-frequency processes. Although wave forces are included in this study, their effect in deep water is secondary when compared with other driving forces.

3.4 Initial and Boundary Conditions

Initial conditions, such as temperature and salinity, should be specified as accurately as possible. However, when “spinning-up” the model, the model’s internal processes replace the initial conditions and a more accurate representation of the environment is obtained. The “spin-up” time can be shortened by specifying accurate initial conditions;

nevertheless, the model still needs to be “spun-up” to reach stability and rid the initial transient data.

Specification of the proper boundary conditions determines the overall success of the model. The boundary conditions applicable to this study include: bathymetry, tides, temperature and salinity, waves, and meteorological information. A brief description of all boundary conditions used to drive the model is provided below.

3.4.1 Bathymetry

The bathymetry is obtained from combined GEODAS and SHOALS data which is regridded in a curvilinear orthogonal coordinate system. The curvilinear orthogonal coordinate system increases the model’s resolution near the coast, where complex hydrodynamic processes occur, and lowers the resolution near the open boundaries. Using a grid such as this provides the ability for the model to give an effective representation of the coastal ocean environment while remaining computationally efficient (Blumberg *et al.*, 2000).

GEODAS is an interactive database management system developed by the National Geophysical Data Center (NGDC) for use in the assimilation, storage, and retrieval of geophysical data. The GEODAS software is being used with several types of data including marine trackline geophysical data, hydrographic (bathymetric) survey data, aeromagnetic survey data, multibeam bathymetric data, and gridded bathymetry/topography. The seafloor data between the latitudes 64° north and 72° south, which encompasses the Hawaii region, are from the work of Smith and Sandwell

(1997). Derived from satellite altimetry observations combined with quality-assured shipboard echo-sounding measurements, this data represents the deeper areas that SHOALS does not accurately represent.

Bathymetric data from the SHOALS project was obtained using airborne LIDAR bathymetric mapping. Airborne LIDAR bathymetric mapping, otherwise known as Airborne LIDAR Hydrography (ALH), uses state-of-the-art Light Detection And Ranging (LIDAR) technology to rapidly and accurately measure seabed depths and topographic elevations. ALH has the ability to rapidly survey over large areas, far exceeding the capabilities and efficiency of traditional survey methods. Since ALH uses light to measure water depth, accurate results are obtained in water depths less than 2 to 3 times the measured secchi depth. In Hawaii the secchi depth is quite large giving ALH the ability to provide data up to a depth of about 40 meters. In more turbid waters the maximum light penetration depth is reduced which in turn decreases the maximum allowable ALH survey depth. SHOALS provides high resolution data to represent the areas of the coastal ocean that are not accurately represented by GEODAS data.

3.4.2 Tides

The tidal boundary conditions are obtained from the TPXO6 global inverse tide model (Egbert, 1997; Egbert and Erofeeva, 2002). The tidal elevation boundary conditions are not taken directly from the TPXO6 tide model, due to its coarse resolution, but are obtained from the results of a two-dimensional barotropic ECOM simulation. This simulation is run for the entire Hawaii region using the model developed for the first

layer of the work completed by Lewis *et al.* (2001).

TPXO6 is a medium resolution, $1/4^{\circ} \times 1/4^{\circ}$, global inverse tide model whose domain includes ocean cavities under floating ice shelves. The principal assimilated data set is TOPEX/Poseidon satellite radar altimetry between $\pm 66^{\circ}$ latitude (Egbert *et al.*, 1994). However, the model also includes patches for various “coastal” oceans, including the Antarctic (Podman and Erofeeva, 2004). TPXO6 is one of the most accurate global tidal solutions, particularly for high latitudes, since it utilizes recent Antarctic grounding line information and Antarctic and Arctic tide height data.

3.4.3 Temperature and Salinity

The temperature and salinity open boundary conditions are obtained from the Modular Ocean Data Assimilation System (MODAS). This assimilation model provides ECOM with the most accurate description of the water column’s properties along the open boundary. MODAS is a variable resolution, from $1^{\circ} \times 1^{\circ}$ in the open ocean to $1/8^{\circ} \times 1/8^{\circ}$ near the coast, global model that creates an analysis of the three-dimensional temperature and salinity structure in the ocean through the combination of satellite and in-situ data (Fox *et al.*, 2001). This combination of data results in a “dynamic climatology”, one of the most significant components of MODAS. Conventionally, the historical data are condensed into an average profile. However, information such as surface temperature and dynamic height can be remotely extracted and correlated to variations in the subsurface temperature. Salinity can then be estimated from derived relationships of temperature at each depth. The resulting dynamic climatology starts with a simple mean profile of

temperature and salinity which is then corrected using height and temperature measurements from space-borne satellites. Since the model is based on a tuned climatology, transient features such as mesoscale eddies and internal waves will most likely be missed by the model.

3.4.4 Waves

Wave information, such as significant wave height and direction, are used as the surface boundary condition. To obtain realistic estimates of the necessary wave information for a given bathymetry, wind field, water level, and open boundary wave field, the numerical wave model SWAN (Simulating WAVes Nearshore) is used. This SWAN model is a third-generation stand-alone (phase-averaged) wave model for the simulation of waves in waters of deep, intermediate, and finite depth (Ris, 1997; Booij *et al.*, 1999). SWAN is also suitable for use as a wave hindcast and forecast model. Since SWAN is a nearshore wave model, and not a global wave model, it requires input from a global wave model so that swell, combined with local wind waves, can be accurately modeled in the nearshore environment. SWAN obtains its open boundary conditions from the global wave model WAVEWATCH III (WW3) (Tolman, 2002; Vandemark *et al.*, 2002).

3.4.5 Meteorological Information

- * Meteorological information, such as atmospheric pressure, wind velocities, and surface heat fluxes is obtained from NOAA's National Centers for Environmental Prediction (NCEP). The NCEP acquires its meteorological information from their Regional Spectral Model (RSM) and provides a 48 hour atmospheric forecast with a 10 km spatial

resolution (Wang *et al.*, 1998). The RSM physics include: short- and longwave radiation with diurnal variation, radiation-cloud interaction, a surface layer with planetary boundary layer physics, gravity wave drag, simplified Arakawa-Schubert convective parameterization scheme, shallow convection, large-scale precipitation, and some hydrological processes (Kanamitsu, 1989).

Chapter 4. Field Measurements

4.1 The Experiment

On April 20, 2005 four drogues were deployed and twelve CTD (Conductivity Temperature Depth) casts were conducted near the Sand Island outfall (Sea Engineering and OCEES, 2005). Continuing the work of Kincaid (2005), the drogues were all deployed to monitor the Lagrangian currents and track the generated plume. Of the four drogues deployed, two of these were intelligent drifters and two were “window curtain” drogues. The two intelligent drifters used were an Autonomous Profiling Vehicle (APV) and an Autonomous Profiling Equipment Carrier (APEC). These devices are similar in operation in that they perform a specific programmed mission. The mission tasks are determined by preset information such as variables to sample, sampling rate, mission duration, and mission type; mission types range from a bottom bounce type trajectory to freely drifting. Furthermore, while these Autonomous Profiling Units (APUs) drift they have the ability to collect temperature, salinity, and depth information.

The APUs were programmed to descend to the approximate depth of the known plume, for the APEC, and to the density associated with the plume, for the APV. After reaching their working depth, the APUs became neutrally buoyant and freely drifted until recovery. While drifting, the APUs collected temperature, salinity, and depth information at preset sampling frequencies. In addition to the sampled data, CTD casts were also performed at various locations along the traveled paths. The “window curtain” drogues, Curtain1 and Curtain2, drifted at preset depths of 50 and 55 meters respectively.

4.2 The Results

The “window curtain” trajectories, shown in figure 5, represent the simplest of trajectories observed in this study due to their two-dimensional nature. The trajectories corresponding to Curtain1 and Curtain2 are shown in blue and red. Figures 6 and 7 depict the APU horizontal and vertical trajectories respectively, the red represents the APV and the blue represents the APEC. It should be noted that the marked locations in figures 5 and 6 display the days past January 1, 2005 referenced to the Universal Time Zone (UTZ). Details on the unmarked APU and “window curtain” trajectory locations, as well as the marked, can be found in Appendices A thru D.

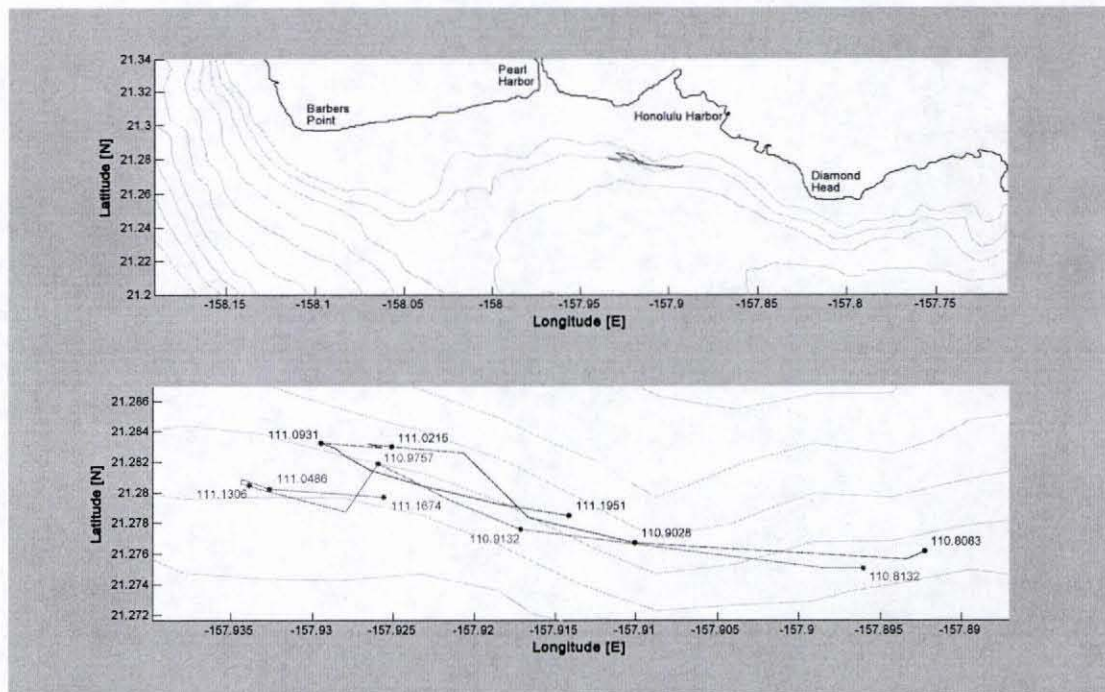


Figure 5: Curtain1 [Blue] and Curtain2 [Red] Trajectories

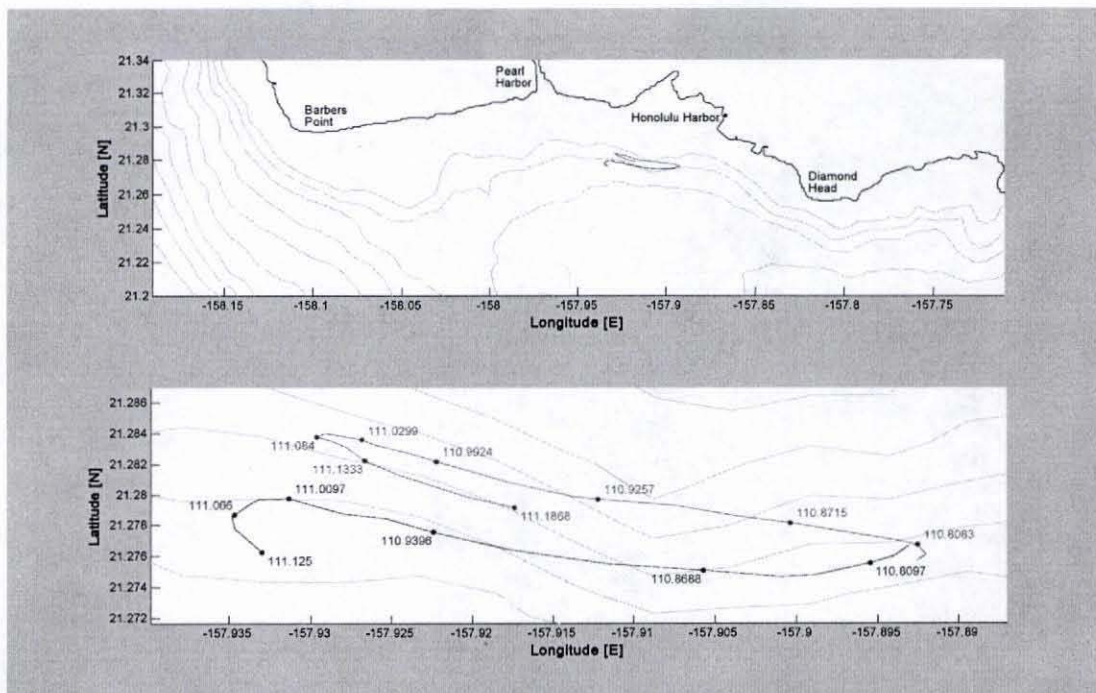


Figure 6: APEC [Blue] and APV [Red] Horizontal Trajectories

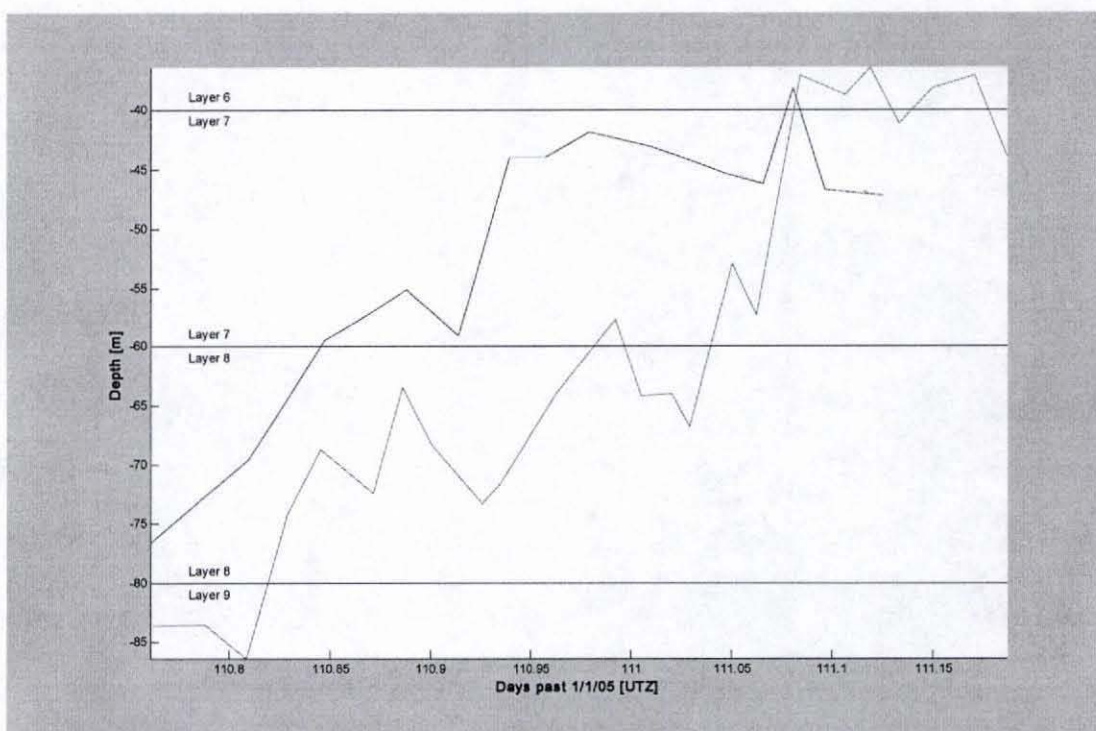


Figure 7: APEC [Blue] and APV [Red] Vertical Trajectories

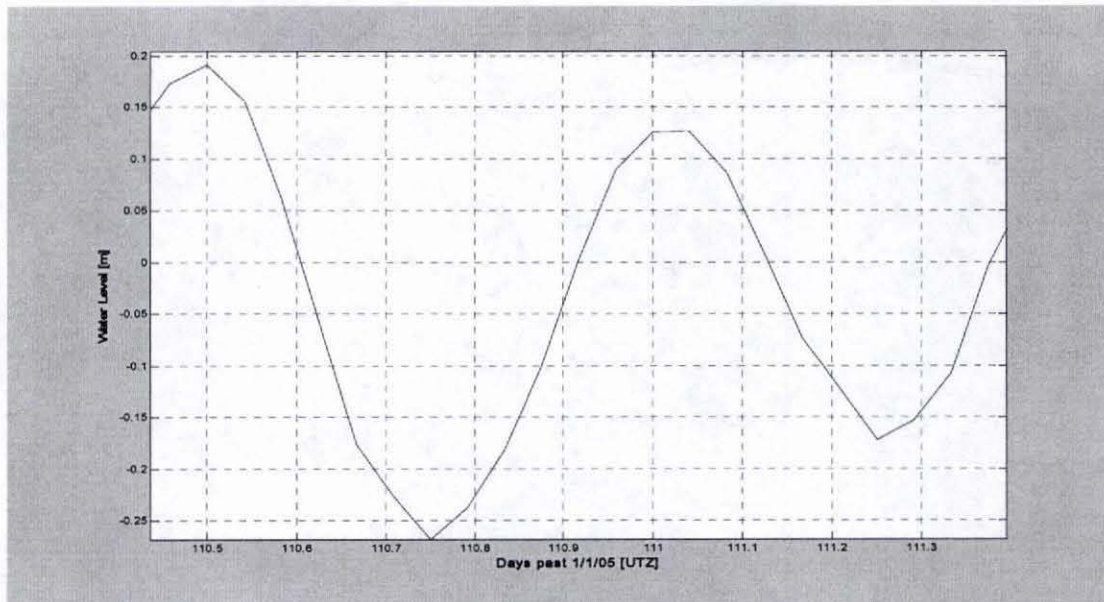


Figure 8: Honolulu Harbor Measured Water Level

It is interesting to note that the APUs both experience tidally driven elliptical trajectories. This fact is demonstrated using figures 6 and 8. Figure 8 represents the water levels measured at the nearby Honolulu Harbor tide station, shown in figures 5 and 6, during the entire day of April 20, 2005 in Hawaiian Standard Time (HST) referenced to the Mean Sea Level (MSL). The abscissa of figure 8 represents the days past January 1, 2005 UTZ. Comparing the two-dimensional trajectories with the measured water levels provides a graphic representation of the previously described tidally driven circulation pattern of this area. On flood tide the APUs drifted toward Barbers Point and on ebb tide the direction reversed and the APUs drifted toward Diamond Head; furthermore, the current speeds range from 12 to 50 cm/s during mid-tide. It is also interesting to note that as the tide neared slack, the velocities of the APUs decreased which further demonstrates the significant impact tides have on currents in the Hawaii region.

On a more realistic side, the “window curtain” trajectories, shown in figure 5, capture the randomness associated with the nearshore currents of this region. Although the trajectories of Curtain1 and Curtain2 are influenced by the tide, they both experience deviations from their tidally driven elliptical trajectories. These deviations can possibly be attributed to their coupling with the surface; however, the complex dynamics associated with the regions nearshore flow is a more reasonable explanation. The model results, described in the next section, will be used to qualitatively explain these deviations as well as the seemingly more predictable trajectories of the APUs. Moreover, the collected CTD data will be presented and statistically compared with the model results to determine the “realism” of this coastal ocean model.

Chapter 5. Model Evaluation

5.1 Model Preparation

Using a curvilinear orthogonal coordinate system, the model grid spacing, shown below in figure 9, was set at 2-3 km around the open boundaries to roughly 1-2 km around the shoreline of Oahu. Furthermore, the model domain extends from approximately 20° to 23° north latitude and 156.5° to 159.5° west longitude. The domain extends well beyond the coast of Oahu to ensure that locally generated internal wave processes are accurately modeled. Lastly, the model was “spun-up” from April 1st at 1000 GMT to April 20th at 1800 GMT before employing the model’s particle tracking feature.

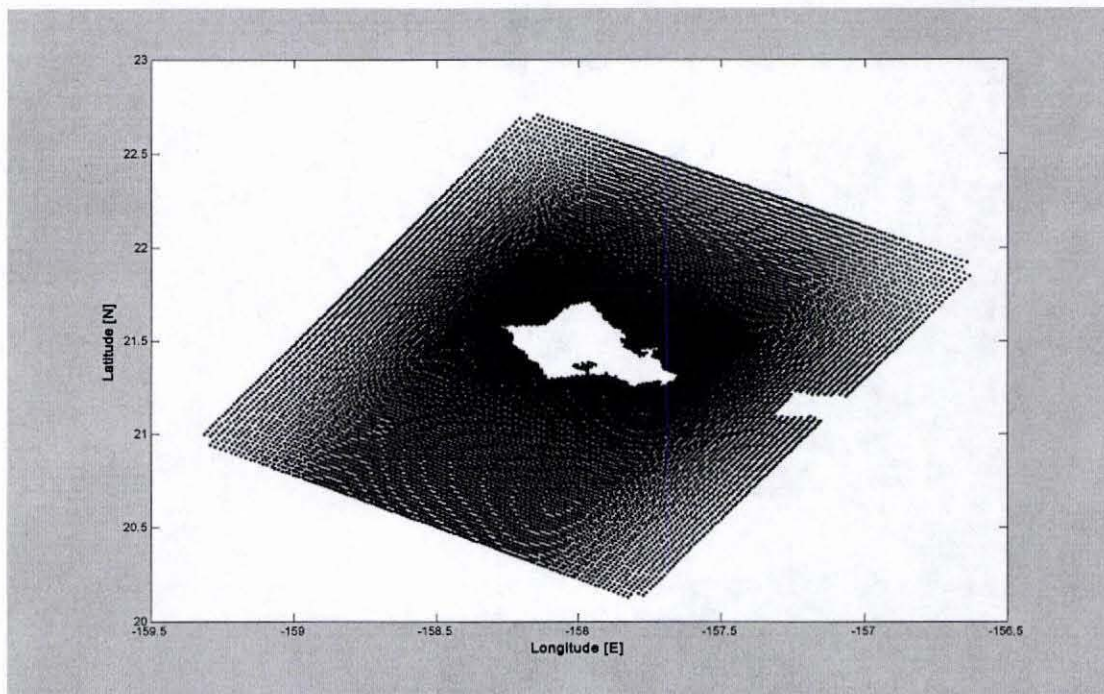


Figure 9: Curvilinear Orthogonal Model Grid for Oahu, Hawaii

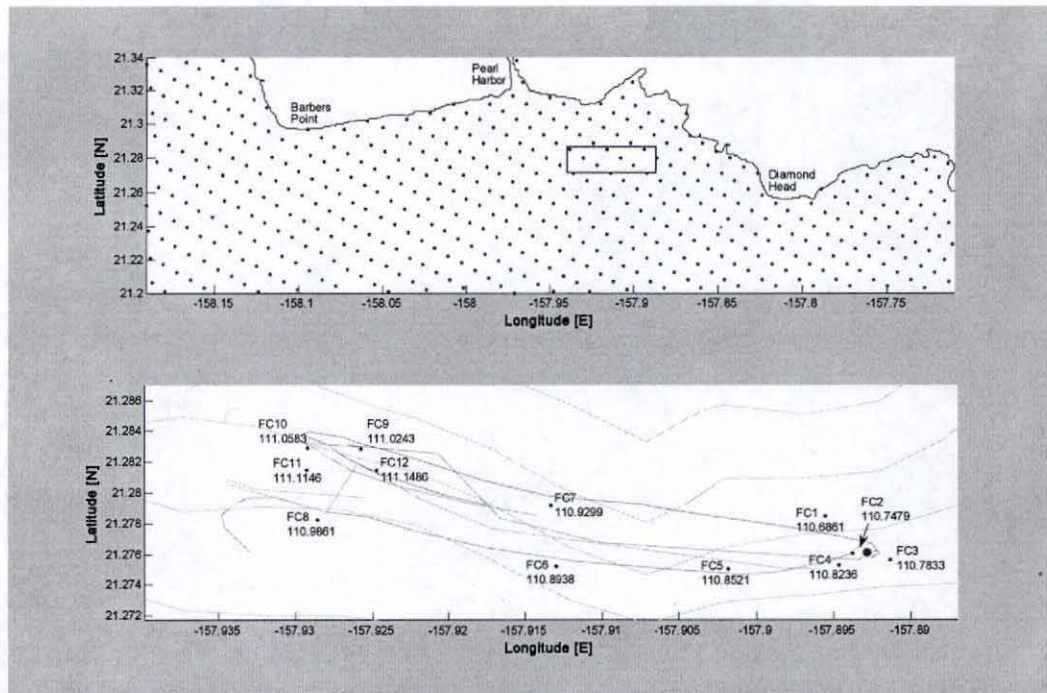


Figure 10 : Field Study Domain and Grid Spacing

The particle tracking feature was engaged on April 20th at 1800 GMT, or 8:00 A.M. HST. The conservative tracer, or particle tracking feature, was emitted into the water column by the virtual diffuser for one hour, between 1800 GMT and 1900 GMT. Figure 10 shows both the model grid spacing near the study area, designated by the red box, and the location of the virtual diffuser relative to the deployed drogues and field casts, shown as the heavy red dot between FC2 and FC3. The location of the virtual diffuser was taken as the grid cell and layer at which the drogues were located nearest 1800 GMT; the depth associated with this position in the model grid is 362.23 meters. Although the average depth of the drogues at this time is at the lower end of layer 9, figure 7 shows that the APV was only in layer 9 for a limited duration giving reason enough to use layer 8 as the location of the virtual diffuser between 1800 and 1900 GMT.

The temperature and salinity of the tracer discharge were obtained from CTD field cast 2 due to its proximity to the drogues at 1757 GMT (CTD field cast details can be found in Appendix E). The temperature and salinity values, 24.59° C and 34.92 PPT respectively, were taken as the average values in layer 8, between 60 and 80 meters, on the descent of CTD field cast 2. The concentration of the tracer was set to 1000 PPM with a 0.1 m³/s influx for the hour of tracer discharge. In order to attain this desired inflow for the entire hour, the inflow was linearly ramped up from 0 m³/s to 0.1 m³/s between 1754 GMT and 1800 GMT. Conversely, the inflow was linearly ramped down from 0.1 m³/s and 0 m³/s between 1900 GMT and 1906 GMT.

Table 1: Drifter Information

Drifter	Time [GMT]	Longitude [E]	Latitude [N]	Depth [m]
APEC	1816	-157.8931	21.2766	76.6110
APV	1818	-157.8926	21.2757	83.6535
Average	1817	-157.8928	21.2761	80.1322

5.2 Model Results

The model results, shown in red, are compared with the collected field data, shown in blue, to determine the model's capabilities and limitations. The variables of interest to this study include: water level, temperature and salinity (sound speed), current velocities, and conservative tracer concentrations. The model output values are taken as the hourly averages for each grid cell. The output time domain extends from April 20th at 1000 GMT to April 21st at 1000 GMT (or the entire 20th day of April referenced to HST).

5.2.1 Water Level

The water levels predicted by the model are compared with the water levels measured by the Honolulu Harbor tide station. The Honolulu Harbor tide station, station number 1612340 of NOAA's National Water Level Observation Network (NWLON), was used due to its proximity to the location of the deployed drifters. The tide station, with geographical coordinates of 21.3067° N and 157.8667° W, sits directly next to the coast in Honolulu Harbor where the resolution of the model is poor. Nevertheless, the hourly measured heights in meters, with respect to the mean sea level (MSL), are compared with the water levels computed by the model, shown below in figure 11.

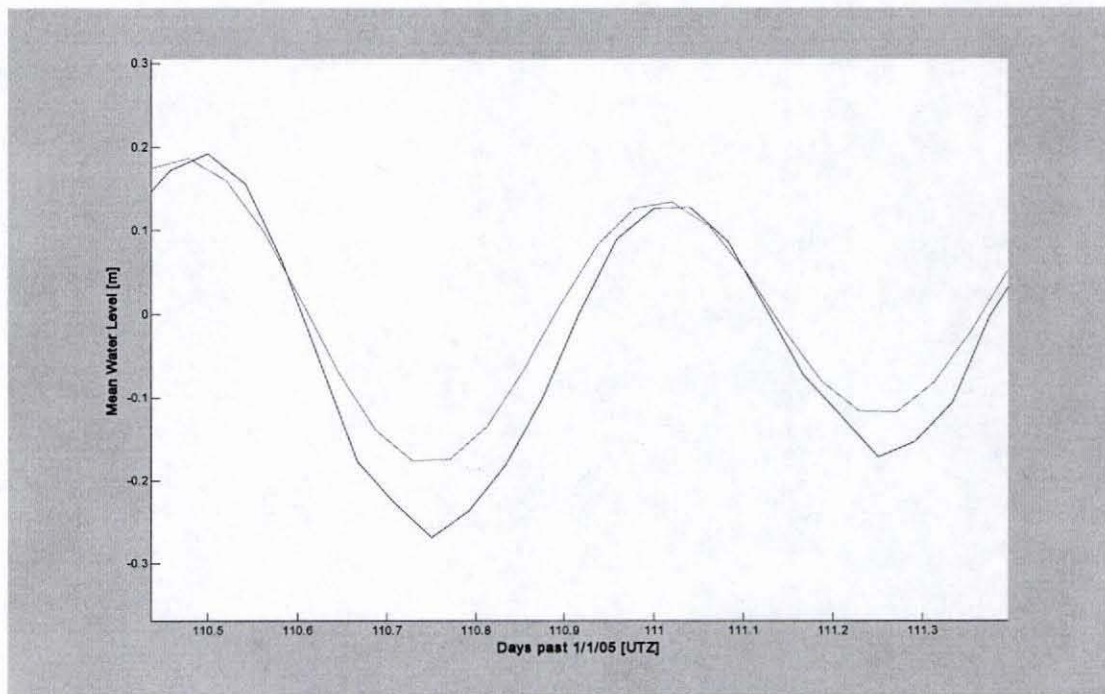


Figure 11: Honolulu Harbor Tide Comparison

As seen in figure 11, the simulated water levels compare favorably with measured water levels. This statement is clearly evident when looking at the statistical comparisons shown below in table 2. The trend of the approximated water levels almost perfectly matches that of the measured water levels, made apparent by both the graphical and statistical (correlation coefficient) comparisons. Furthermore, the average error is minimal, less than 5 centimeters. An animation of the simulated water levels in Mamala Bay for the period of study, named **tide.avi**, is included in the accompanying compact disc.

Table 2: Water Level Correlation and Average Error

Correlation Coefficient	Average Error [m]
0.9908	0.0425

5.2.2 Temperature and Salinity

The temperature and salinity profiles measured during the descent of each of the twelve CTD casts are graphically compared with the corresponding profiles predicted by the model, shown in Appendix E. The sound speed profiles, shown with their representative temperature and salinity profiles, were computed using the 1983 UNESCO polynomial given by Fofonoff and Millard (1983). The descent data in each profile was filtered using a median filter with a 5 point crossing window. The filtered data was then bin averaged using bins corresponding to each of the model's depth layers. Statistical descriptions of the data, such as correlation coefficients and average errors, were then computed using this bin averaged filtered data and are shown in Appendix F.

To help draw conclusions about the model's capabilities, all filtered data has been combined to create a single measured profile. This technique is feasible since all CTD casts have been performed within approximately 2 km of each other (roughly the spatial resolution of the model) over a period of less than 12 hours. This combined dataset was then bin averaged for each of the model's layers and an average deviation for that bin was obtained. This process was repeated for the results obtained from the model. With a 95% confidence interval, figure 12 shows the upper and lower bounds of the measured and predicted statistical profiles for the combined datasets.

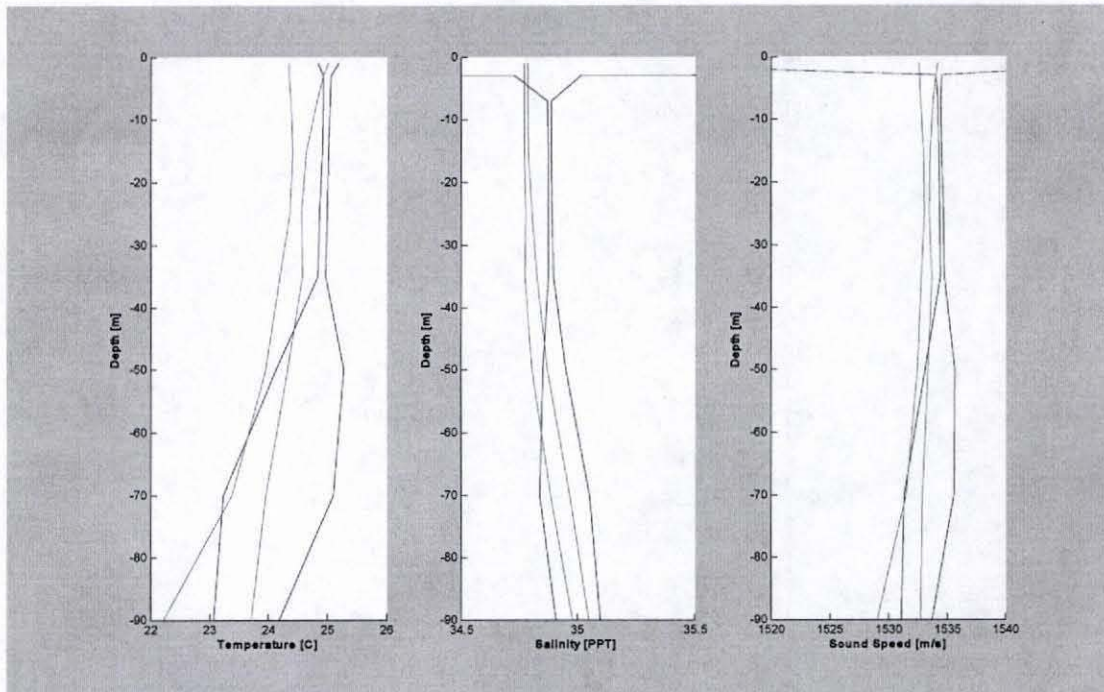


Figure 12 : Combined Field Cast Statistical Comparison

It can be seen from the above figure that the model underpredicts the measured profiles for temperature, salinity, and sound speed. However, the model does realistically capture the variability of these properties as they exist below the ocean's upper layer. The

variability of both the model results and the measured data between 40 and 90 meters imply structural deviations between casts, which can possibly be attributed to strong mixing processes. The minimal spread in both the measured data and model results between 40 meters and below the upper layer of the water column imply stability. Interestingly, the major discrepancy between the measured data and the model's results is in the upper layer of the water column. The variability of the model in this surface layer is minimal, however, the measured data, especially the salinity data, experiences large deviations in this layer. These large deviations in the measured results can possibly be attributed to the strong stratification of the water column.

The table below statistically compares the combined measured and modeled results. It is noticed that only the temperature profile simulated by the model favorably agrees with measured results throughout the sampled water column. The descriptive capabilities of the model near the surface for salinity and sound speed are poor. However, when comparing the data outside the upper layer of the water column, all properties approximated by the model favorably agree with the measured properties. Therefore, the model realistically describes environmental properties below the surface layer, or below 2 meters.

Table 3 : Combined Field Cast Statistics

	Includes Layer 1		Without Layer 1	
	Correlation Coefficient	Average Error	Correlation Coefficient	Average Error
Temperature	0.9936	0.1023	0.9946	0.0963
Salinity	0.2643	1.6131	0.9943	0.0424
Sound Speed	0.1658	1.8615	0.9811	0.1911

5.2.3 Eulerian Circulation

The modeled circulation of Mamala Bay is qualitatively compared with documented observations. Animations of the modeled currents for layers 7 and 8 are presented in **currents.avi**. First, a general picture of the overall circulation is analyzed to determine apparent validity of the model. Then, since the primary driving forces of the currents in the bay are due to tidal and low frequency processes, the tidal current ellipses approximated by the model are compared with observations made in this area. Following these comparisons, the density structure of Mamala Bay, specifically the isopycnals near the mouth of Pearl Harbor, is examined to determine if the model captures the strong mixing and baroclinic currents observed in the area.

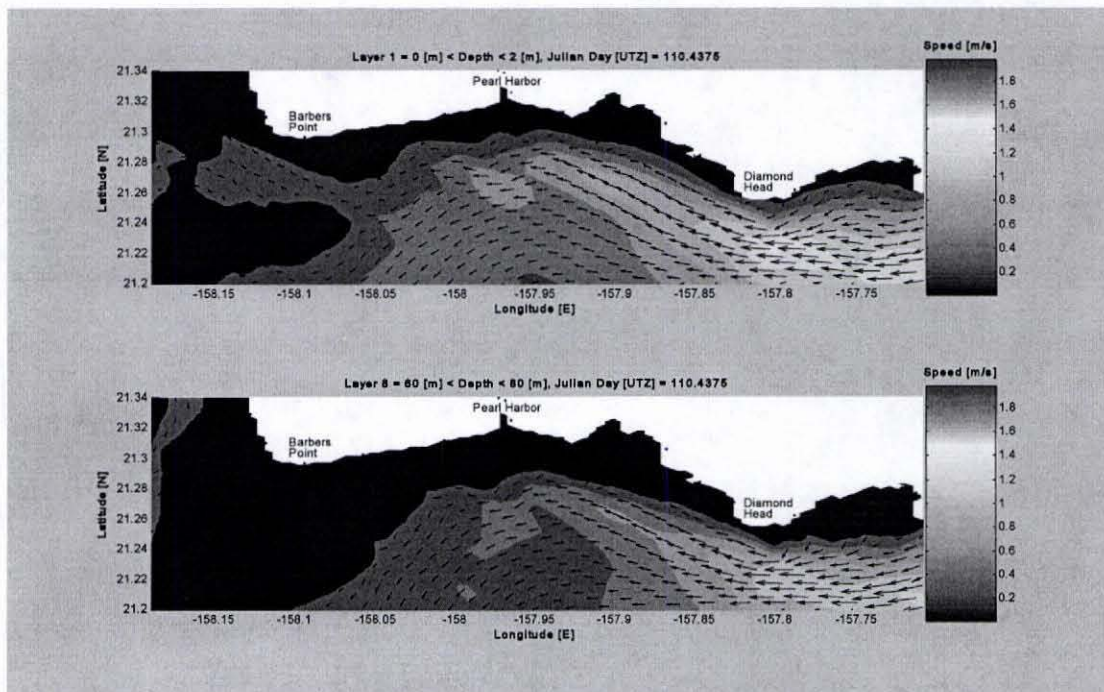


Figure 13 : Mamala Bay Current Structure

Figure 13 shows the current structure in Mamala Bay both at the surface (between 0 and 2 meters) and at depth (between 60 and 80 meters). It should first be noted that the model reveals a significant difference between currents at the surface and currents at depth. Because the model simulates significant currents at depth, and the flow in the bay is dominated by low frequency processes, this slight decay of current amplitude with depth is most likely due to the rapid decay of the wind generated current with depth. Being the first half of the year, the model also agrees with observations stating that the mean flow is directed out of the bay at both Diamond Head and Barbers Point. Moreover, the model realistically captures the strong currents experienced at Diamond Head and the western-propagating flow in the bay.

The incredibly strong and deeply penetrating current amplitudes seen in the model results near Diamond Head have also been observed in the field by Hamilton *et al.* (1995). This phenomenon is possible considering a western propagating subtidal flow with amplitude exceeding 60 cm/s. Constructive interference of these strong subtidal currents with strong tidal currents could result in the current amplitudes exceeding 100 cm/s. Current flow tidal dependencies are examined to determine the feasibility of this explanation.

Figure 14 depicts both flood and ebb tide events and is used to demonstrate the strong coupling between coastal currents and tidal phase. During flood tide, shown in the upper plot, the current amplitudes near Diamond Head are significantly stronger than they are during ebb tide. This tidal signature is further investigated using tidal decomposition (Pawlowicz *et al.*, 2002).

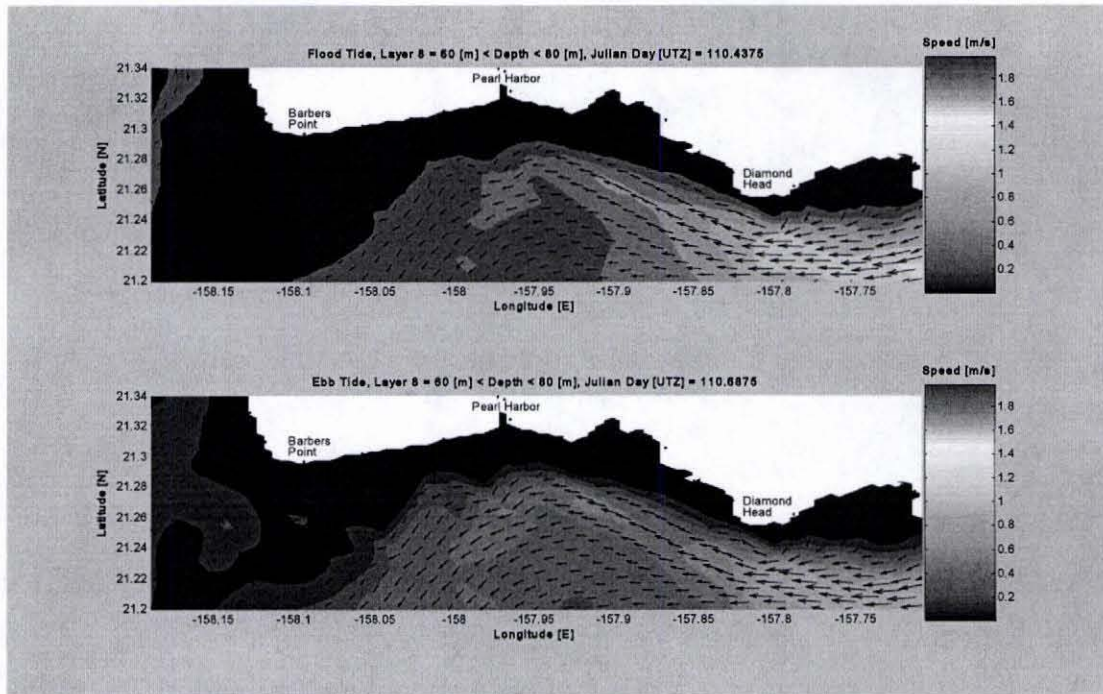


Figure 14 : Flood and Ebb Currents

With a 95% confidence interval, figure 15 depicts the modeled M2 tidal current ellipses and their representative phases, shown by the black line in the center of the ellipse. The locations and properties of these current ellipses can be found in Appendix G. The red ellipses represent clockwise rotation, while the blue signify counterclockwise rotation. The K1 tidal current ellipses have not been computed due to the model's limited run duration. Also, since these tidal current ellipses are calculated using data for only one day, the magnitudes and directions depicted have large associated errors, shown in Appendix G. However, these current ellipses do show the tidal current flow in the bay for the day of interest.

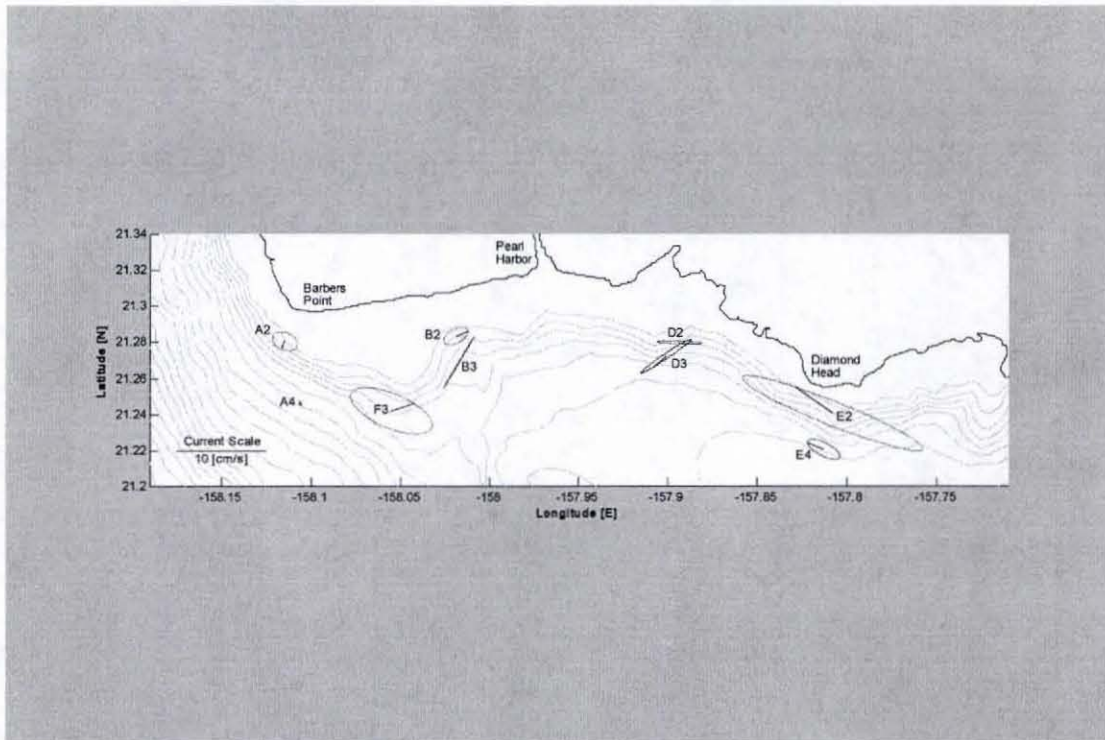


Figure 15 : M2 Tidal Current Ellipses

It can clearly be seen that the model results favorably agree with observations made by Hamilton *et al.* (1995). First, and most noticeably, the tidal current amplitudes are largest near the headlands, exceeding 10 cm/s, and decrease toward the bay center, with amplitudes less than 1 cm/s. As a result, the strong currents near Diamond Head can only be explained by intense subtidal flows exceeding 90 cm/s; this is a possibility since 60 cm/s daily average subtidal flows have been observed in this region of small spatial scale variability. Additionally, the phases of the tidal currents in the eastern part of the bay lead those of the western by nearly 180° . This phase lead is another contributor to the western-propagating flow in the bay. Moreover, the oppositions in phase also suggest that the model captures the opposing tidal currents observed at Diamond Head and Barbers Point.

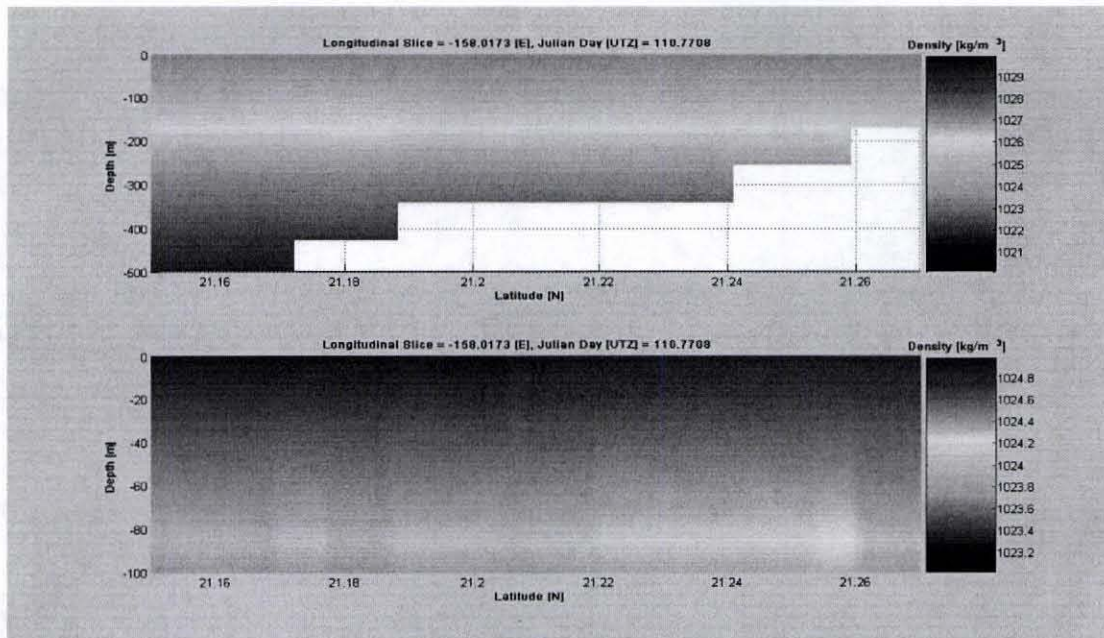


Figure 16 : Mamala Bay Density Structure Longitudinal Slice

The mean offshore flow in the bay between Pearl Harbor and Barbers Point can partially be attributed to the M2 barotropic current, shown in figure 15. However, since the overall mean flow at this point, and outside the mouth of Pearl Harbor, is significant at all times (see figure 13), there must be another major component contributing to the current other than tides (too deep for wind and waves). When looking at a longitudinal slice of the bay's density structure, considerable mixing and horizontal density gradients are noticed, shown in figure 16 (see **density.avi** in the accompanying compact disc for the animation). These horizontal density gradients result in baroclinic flow; the observed baroclinic currents in the bay at this location are strong (as much as 0.5 m/s), often several times in excess of the depth-averaged flow (Alford *et al.*, 2005). Therefore, the model also demonstrates its ability to capture mixing and the significant impact baroclinic currents have on the overall current structure in Mamala Bay.

5.2.4 *Lagrangian Circulation*

A conservative tracer has been chosen as the numerical tool used to virtually track the deployed drogues. This feature is not meant to track the drogues or look at their individual trajectories, rather it is used to provide a statistical representation of where the drogues could possibly travel to in this chaotic coastal ocean environment. Figure 17 shows the modeled tracer concentrations in layer 8, between the depths of 60 and 80 meters, at two different times. The domain encompassing the study area used for the deployed drogues is boxed in red and the location of the virtual diffuser is shown as the red dot. The upper plot in figure 17 shows the tracer leaving the virtual diffuser in a plume with all particles traveling as a group, since this plume is one solid body. Then, looking at the bottom plot in figure 17, it is noticed that the plume that once traveled as a solid body has now broken into several. This is a result of different particles being trapped or swept away by different circulation patterns. The group near the study area most likely is experiencing barotropic elliptical currents, due to their relatively stagnant position. Conversely, the group, or plume, traveling offshore is most likely experiencing the strong baroclinic currents produced by the model and observed in this area. Therefore, the model proves its ability to realistically capture the chaotic horizontal processes observed in the coastal ocean environment.

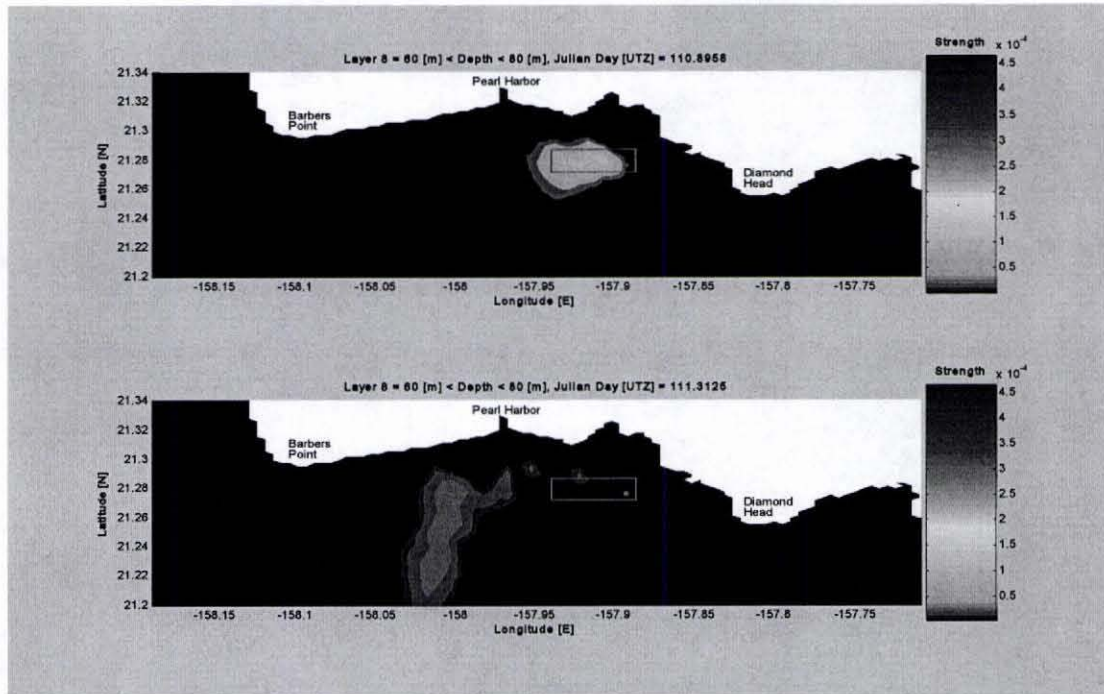


Figure 17 : Virtual Particle Tracking Horizontal Scenarios

Interestingly, it was found that the virtual tracer emitted into the model's eighth layer had a density less than that predicted by the model for that layer. Using the algorithms developed by Fofonoff and Millard (1983), the density of the virtual tracer was found to be 1023.7 kg/m^3 and the density associated with the model at the time and location of tracer release was found to be 1024.3 ; therefore, the tracer is expected to ascend through the virtual water column. Furthermore, the density of the tracer at this time and location is denser than the density associated with layer 6. As a result, the tracer is expected to initially travel, in the vertical direction, between the eighth and seventh layers. After this initial dispersal, turbulent motion in the vertical direction is expected, especially in this region of intense mixing. Figure 18 is used to demonstrate the model's ability to realistically describe Lagrangian vertical motion. It can be seen that the tracer does not

just ascend through the water column, but that it travels between layers due to turbulence and diffusion. Therefore, the model also demonstrates its ability to realistically simulate turbulent and diffusive processes between model layers.

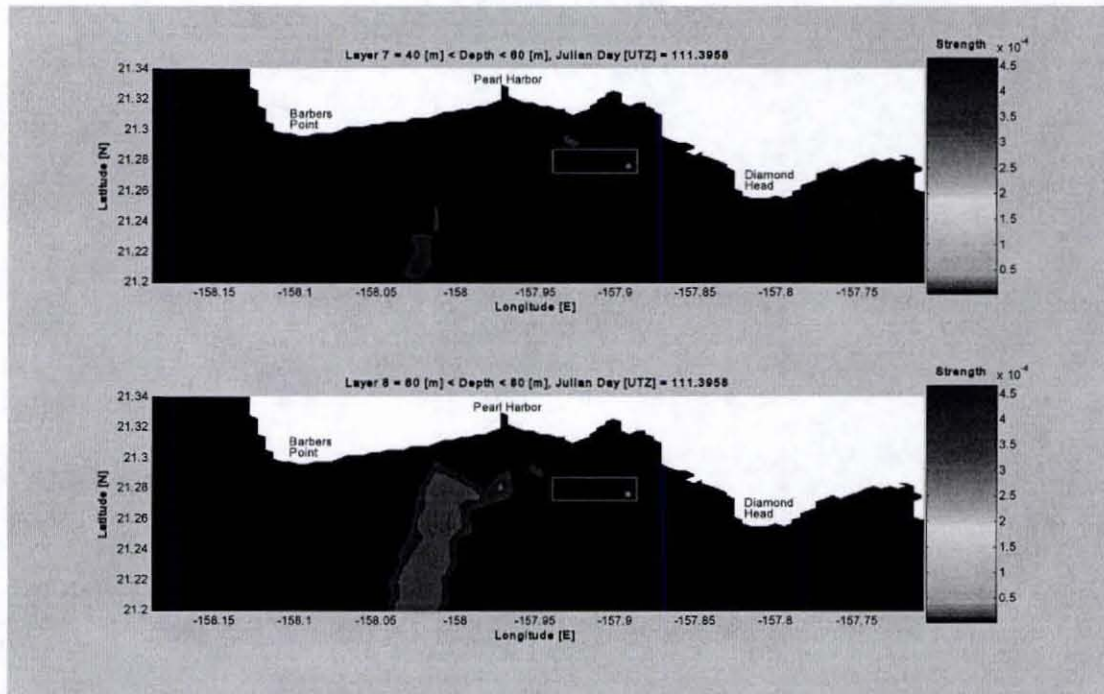


Figure 18 : Virtual Particle Tracking Vertical Scenarios

Although the virtual tracer does not stay in the study area, it does realistically propagate throughout the bay. The complex dynamics associated with this environment result in chaotic motions. This chaos is made evident when the virtual plume separates into several plumes rather than traveling as a whole. Even if additional drogues were deployed in the same area, their trajectories would differ from the trajectories previously described. Animation of the tracer's trajectories for layers 7 and 8 can be viewed in **tracer.avi**.

The trajectories of the deployed drogues are no more representative of the actual Lagrangian currents than the results obtained from the model. There are errors and uncertainties associated with the drogues just as there are with the model. All deployed drogues were connected to a surface float for tracking purposes. Significant drag on a surface float can result in current measurement error; the window curtain drogues would experience currents at shallower depths than expected and the APUs would appear to ascend through the water column. This is only one error associated with the coupling between the drogues and the surface float. The actual dynamics of the drogue trajectories are even more complex; water particles that supposedly travel with the drogue can slip past and not travel with the drogue for the entirety of the study.

To further validate the Lagrangian capabilities of the model, concentration measurements should be taken and compared with the results of a conservative tracer simulation. Using a conservative tracer, such as sulfur hexafluoride (SF_6), would prove beneficial in gathering the necessary Lagrangian data to form statistical conclusions. Moreover, since a tracer would better follow individual particles, the results would provide additional information on the complex current structure experienced in the bay.

Chapter 6. Conclusions

A state-of-the-art coastal ocean model has been evaluated for the island of Oahu, Hawaii. The model's capabilities and limitations have been determined. The Eulerian results, such as water levels and vertical profiles, were first quantitatively compared with field measurements. Then the current structure simulated by the model was qualitatively compared with the known current structure of Mamala Bay. Finally, the results of a conservative tracer simulation were qualitatively analyzed and compared with field measurements to determine the model's Lagrangian capabilities.

The model has demonstrated its ability to realistically describe the coastal ocean environment. It has been able to realistically simulate water levels observed in the bay, with a correlation coefficient above 0.99 and an average error less than 5 cm. Limitations have been observed in the model's ability to simulate the vertical structure of the water column. However, the model does realistically capture the vertical structure of the water column below the surface layer. Average errors decreased by an order of magnitude when not including the surface layer in the analysis; the associated correlation coefficients also significantly improved, increasing from as low as 0.1658 to 0.9811. Major contributors to ocean currents in this area, such as tidal and low-frequency processes, have been realistically reproduced by the model; tidal, subtidal, and baroclinic currents simulated by the model favorably agree with observations. Moreover, the Lagrangian capabilities have realistically demonstrated the complexity and chaotic nature of the coastal ocean environment.

Although the model does not have the capability to predict, it has demonstrated its ability to create a “realistic” virtual ocean environment. Features observed in the simulation represent possibilities that could occur in the real ocean environment. The model does not provide the ability to say that the current near Diamond Head will be flowing in the east-northeast direction with a magnitude of 20 cm/s at 2:00 p.m. on Monday, November 28th; however, it does provide information necessary to know that relatively strong and tidally dependant currents are common near Diamond Head. This capability of the model should be useful to the ocean community in planning operations, conducting virtual training exercises, and performing post mission analysis of at sea operations.

This evaluation demonstrates the feasibility of creating a “realistic” virtual ocean environment. This is an incredible capability that will prove itself immediately useful to the autonomous underwater vehicle (AUV) community. Two significant barriers that presently exist in the autonomous operation of undersea robots are power and control (Office of Naval Research, 2004). Power provides the vehicles with the ability to operate while control facilitates coordinated operations. The combination and efficient use of these necessary components will further increase the mission capabilities of AUVs.

The creation of a “realistic” virtual ocean environment will provide AUV researchers with the ocean on their desktop. This will facilitate the realistic and cost effective test of advanced control algorithms. Historically AUV simulation environments assume current velocities and vertical profiles are statistically identical at all locations, resulting in an isotropic representation (Fossen, 2002). For example, the ocean current used in the Distributed Virtual Environment Collaborative Simulator for Underwater

Robots contains no turbulence and no curl (Choi *et al.*, 2000). This isotropic model representation of the ocean environment is very simple and is not valid in regions where the water column is highly stratified with variable bathymetry, such as the Hawaiian Islands.

Our coastal environment is highly dynamic. When operating AUVs in this environment, the simulation used to validate the design or mission plan should model the external disturbances accurately (Bruzzone *et al.*, 2001). During the course of a single mission, an AUV may experience a variety of environmental conditions such as highly stratified waters, light and variable direction currents, strong and persistent uni-directional currents, among others. Having an idea of these environmental conditions *a priori* will provide the information necessary to create optimal AUV sortie plans. Therefore, this evaluation confirms that a “realistic” virtual environment for autonomous underwater vehicles is feasible.

Appendix A : APEC Location Data

UTZ [day]	Longitude [E]	Latitude [N]	Depth [m]
110.6646	-157.90359	21.27868	0
110.6764	-157.90232	21.27832	0
110.6771	-157.90164	21.27851	0
110.7257	-157.89347	21.27698	0
110.7611	-157.89311	21.27664	76.6111
110.7889	-157.89399	21.27601	72.5617
110.8097	-157.89545	21.27553	69.5390
110.8361	-157.89882	21.27478	62.4423
110.8472	-157.90087	21.27467	59.4601
110.8688	-157.90569	21.27504	57.3139
110.8882	-157.91152	21.27548	55.1204
110.9139	-157.91767	21.27643	59.0533
110.9396	-157.92242	21.27757	43.9773
110.9576	-157.92540	21.27847	43.9941
110.9799	-157.92800	21.27873	41.9072
111.0097	-157.93133	21.27972	43.0681
111.0319	-157.93319	21.27966	44.3988
111.0472	-157.93387	21.27930	45.3593
111.0660	-157.93468	21.27870	46.2507
111.0806	-157.93482	21.27860	38.1945
111.0965	-157.93464	21.27778	46.7453
111.1250	-157.93304	21.27623	47.1826
111.1542	-157.92886	21.27474	0

Table 4 : APEC Location Data

Appendix B : APV Location Data

UTZ [day]	Longitude [E]	Latitude [N]	Depth [m]
110.7069	-157.89497	21.27657	0
110.7625	-157.89264	21.27572	83.6535
110.7882	-157.89205	21.27605	83.5203
110.8083	-157.89253	21.27670	86.3998
110.8292	-157.89355	21.27694	74.1560
110.8451	-157.89562	21.27734	68.6703
110.8715	-157.90033	21.27813	72.4205
110.8861	-157.90352	21.27855	63.4383
110.9007	-157.90734	21.27925	68.2893
110.9257	-157.91220	21.27967	73.2853
110.9347	-157.91364	21.27984	71.5755
110.9632	-157.91782	21.28082	64.0040
110.9924	-157.92223	21.28216	57.7305
111.0056	-157.92409	21.28277	64.1510
111.0208	-157.92601	21.28324	63.9724
111.0299	-157.92687	21.28360	66.7315
111.0507	-157.92838	21.28385	52.9437
111.0625	-157.92912	21.28399	57.2853
111.0840	-157.92966	21.28377	37.0898
111.1063	-157.92870	21.28346	38.6979
111.1188	-157.92788	21.28310	36.4344
111.1333	-157.92669	21.28222	41.1510
111.1500	-157.92454	21.28126	38.1323
111.1708	-157.92020	21.27982	37.1461
111.1868	-157.91739	21.27915	43.8914
111.2104	-157.91449	21.27823	0

Table 5 : APV Location Data

Appendix C : Curtain1 Location Data

UTZ [day]	Longitude [E]	Latitude [N]
110.8132	-157.89606	21.27505
110.8354	-157.89849	21.27509
110.9132	-157.91713	21.27762
110.9410	-157.92172	21.27955
110.9597	-157.92425	21.28100
110.9757	-157.92599	21.28187
110.9799	-157.92800	21.27873
111.0326	-157.93328	21.28024
111.0486	-157.93392	21.28045
111.0653	-157.93446	21.28055
111.0986	-157.93437	21.28086
111.1306	-157.93264	21.28022
111.1674	-157.92561	21.27970

Table 6 : Curtain1 Location Data

Appendix D : Curtain2 Location Data

UTZ [day]	Longitude [E]	Latitude [N]
110.8083	-157.89225	21.27622
110.8278	-157.89341	21.27564
110.9028	-157.91005	21.27675
110.9382	-157.91667	21.27836
110.9951	-157.92071	21.28255
111.0215	-157.92516	21.28297
111.0528	-157.92664	21.28315
111.0903	-157.92572	21.28294
111.0931	-157.92955	21.28326
111.1076	-157.92865	21.28285
111.1181	-157.92804	21.28241
111.1326	-157.92644	21.28147
111.1507	-157.92330	21.28044
111.1722	-157.91858	21.27930
111.1951	-157.91415	21.27850

Table 7 : Curtain2 Location Data

Appendix E : Eulerian Field Data Location Information

Location	Longitude [E]	Latitude [N]	Julian Day [UTZ]
Honolulu Harbor	-157.8667	21.3067	-
FC1	-157.8955	21.2784	110.6861
FC2	-157.8938	21.2760	110.7479
FC3	-157.8913	21.2756	110.7833
FC4	-157.8947	21.2753	110.8236
FC5	-157.9018	21.2750	110.8521
FC6	-157.9130	21.2752	110.8938
FC7	-157.9134	21.2792	110.9299
FC8	-157.9286	21.2782	110.9861
FC9	-157.9257	21.2828	111.0243
FC10	-157.9292	21.2829	111.0583
FC11	-157.9293	21.2815	111.1146
FC12	-157.9248	21.2815	111.1486

Table 8 : Eulerian Field Data Location Information

Appendix E: Field Cast Data Comparisons

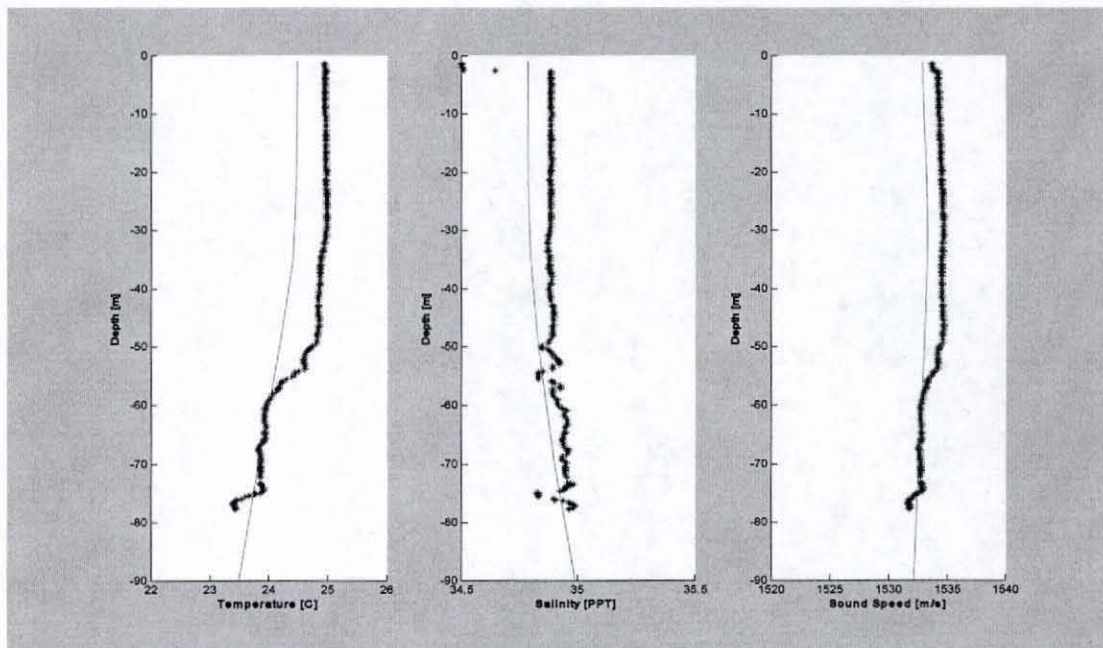


Figure 19 : Field Cast 1 Data Comparison

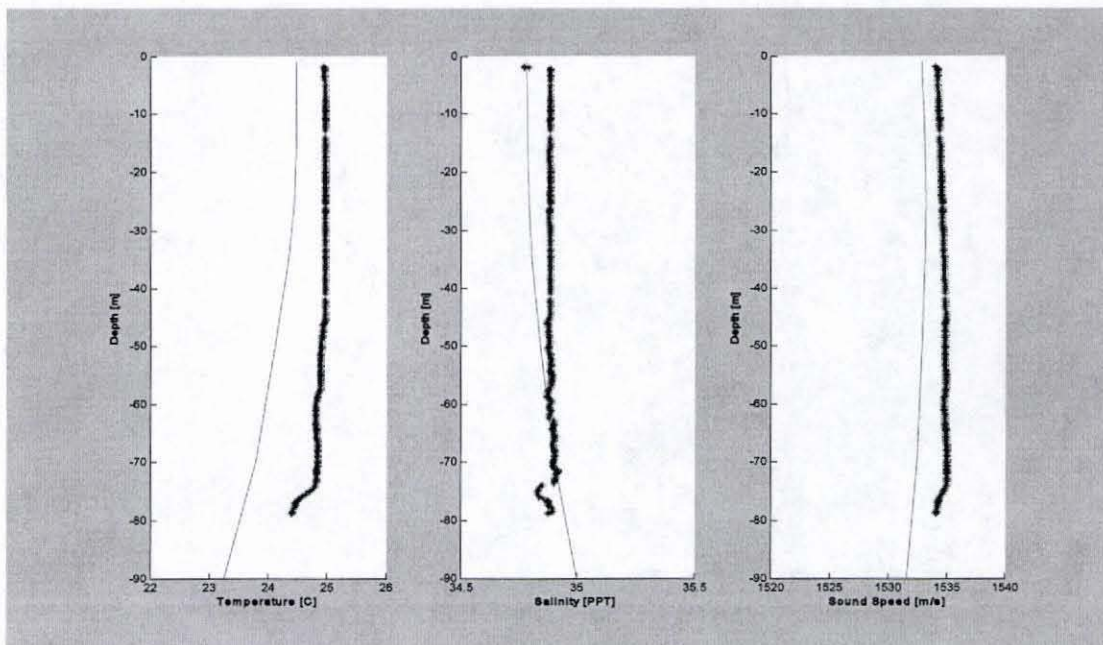


Figure 20 : Field Cast 2 Data Comparison

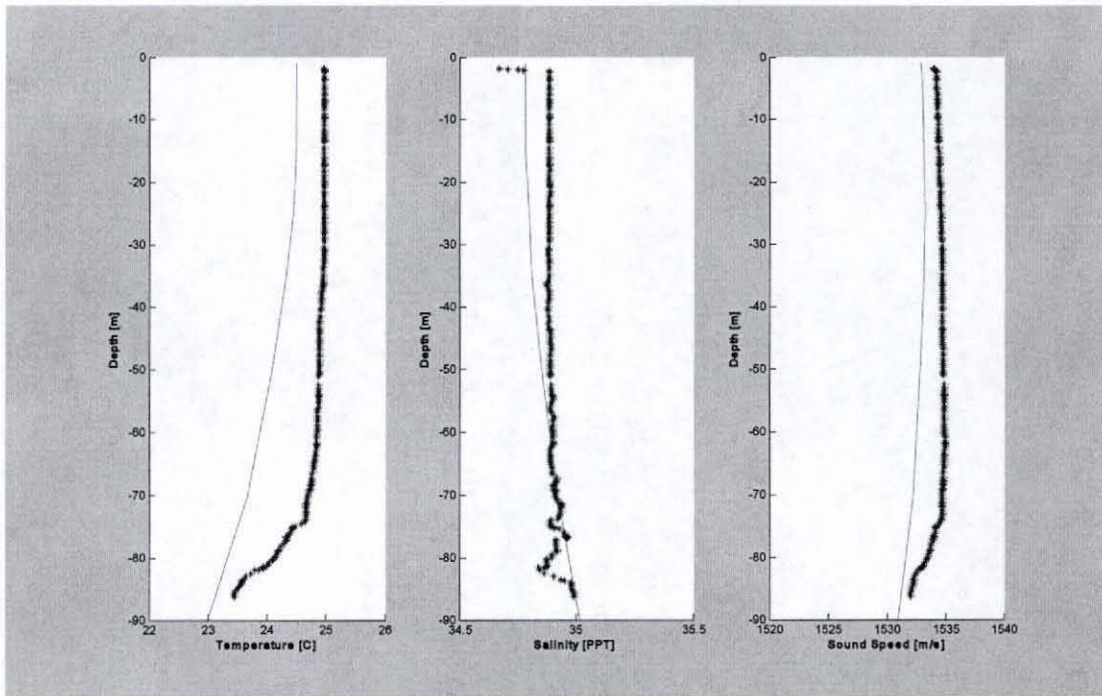


Figure 21 : Field Cast 3 Data Comparison

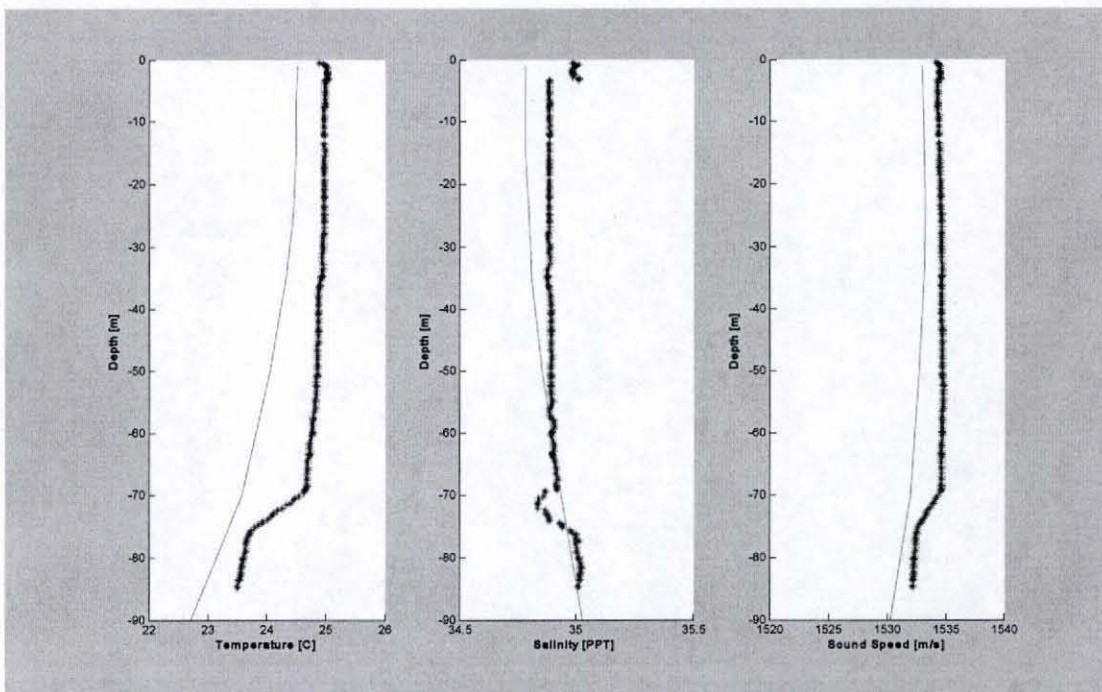


Figure 22 : Field Cast 4 Data Comparison

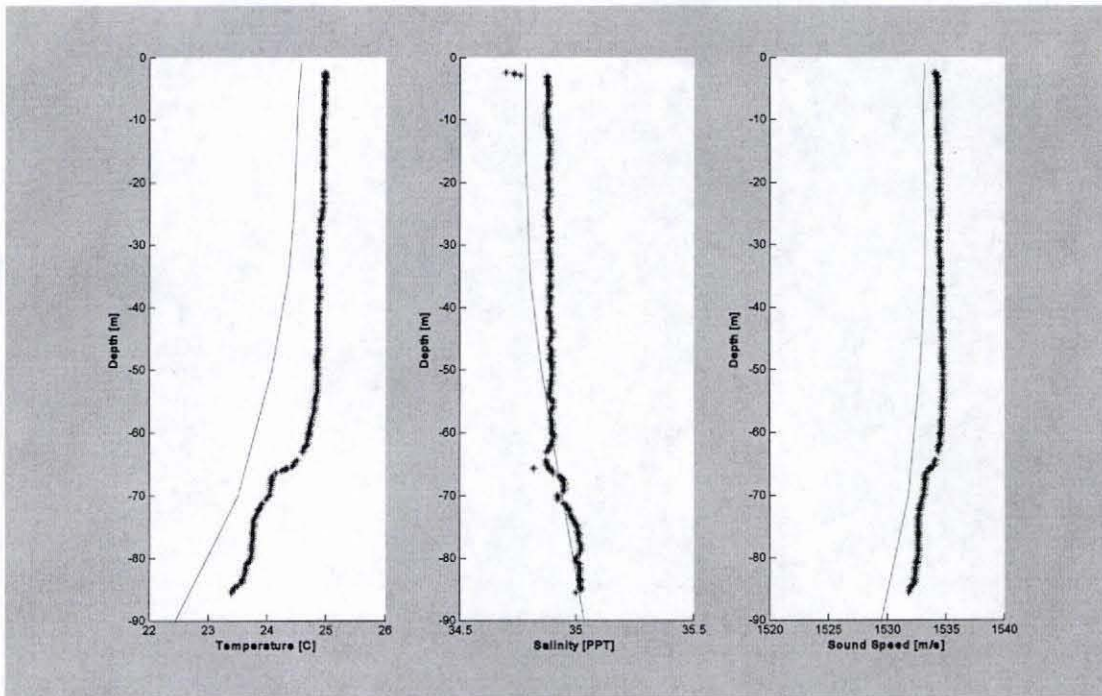


Figure 23 : Field Cast 5 Data Comparison

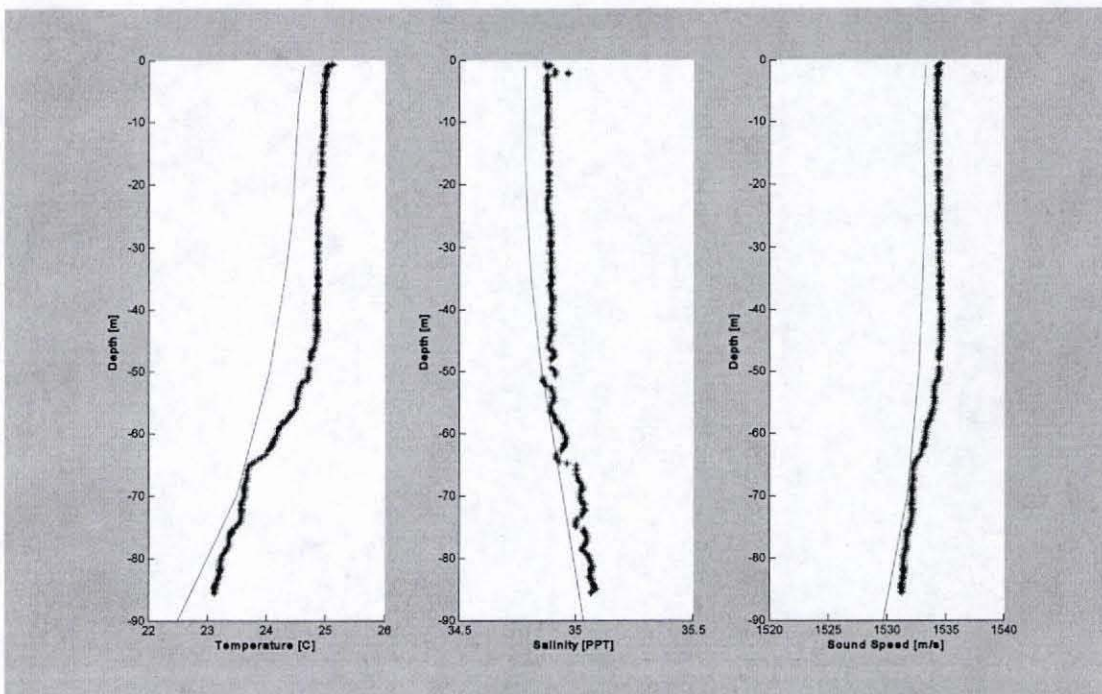


Figure 24 : Field Cast 6 Data Comparison

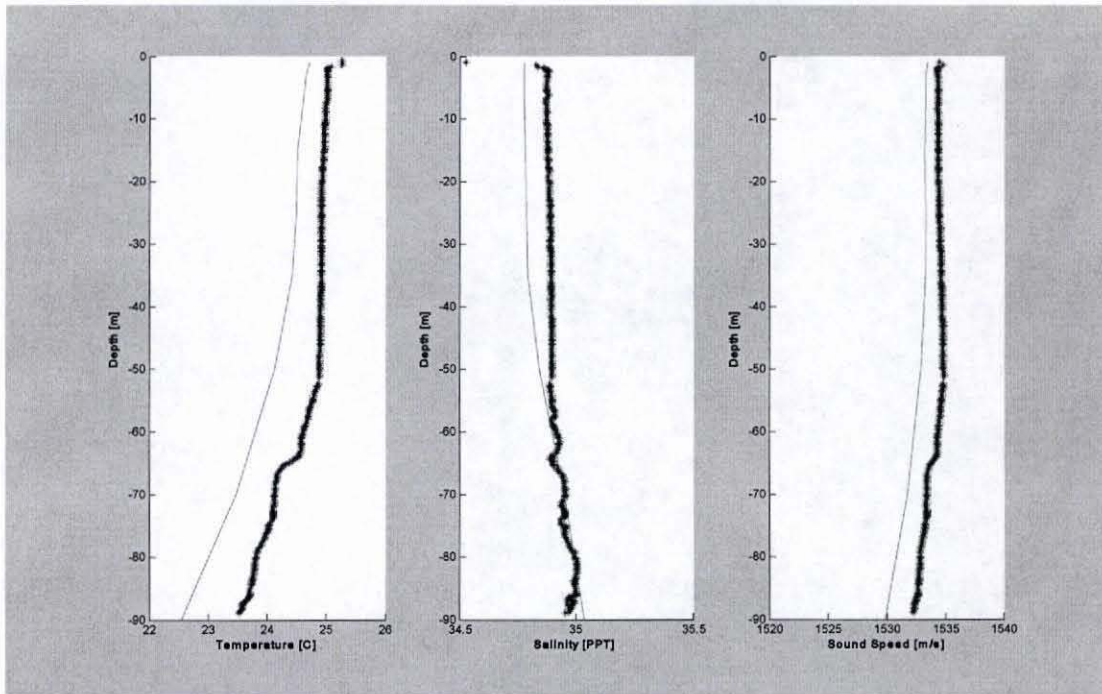


Figure 25 : Field Cast 7 Data Comparison

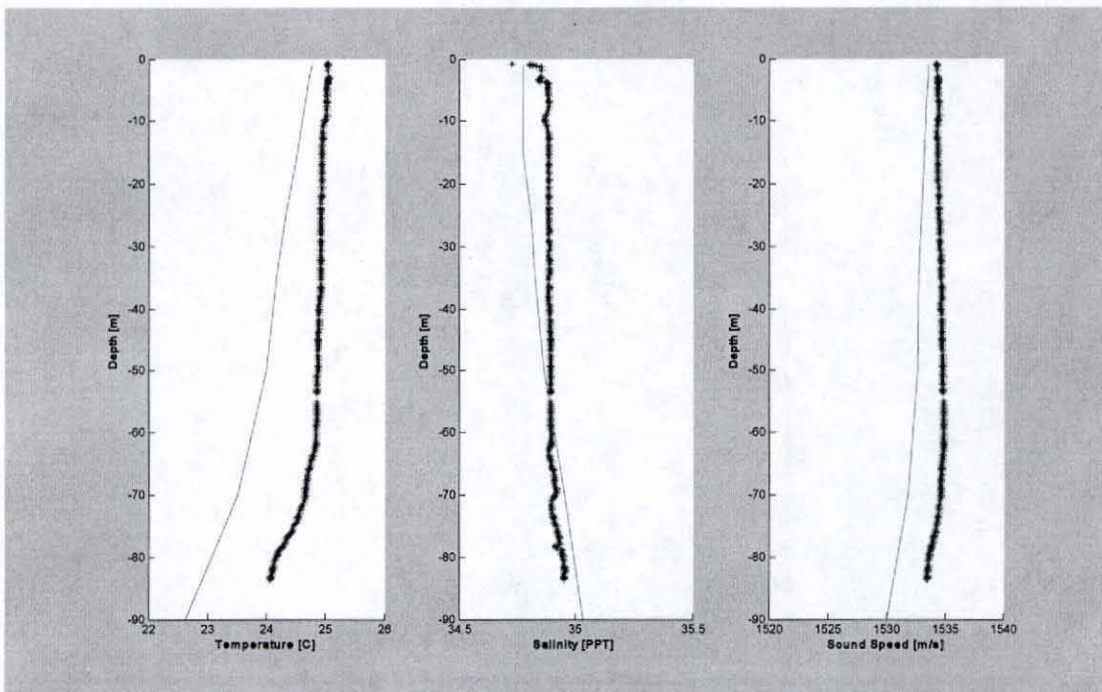


Figure 26 : Field Cast 8 Data Comparison

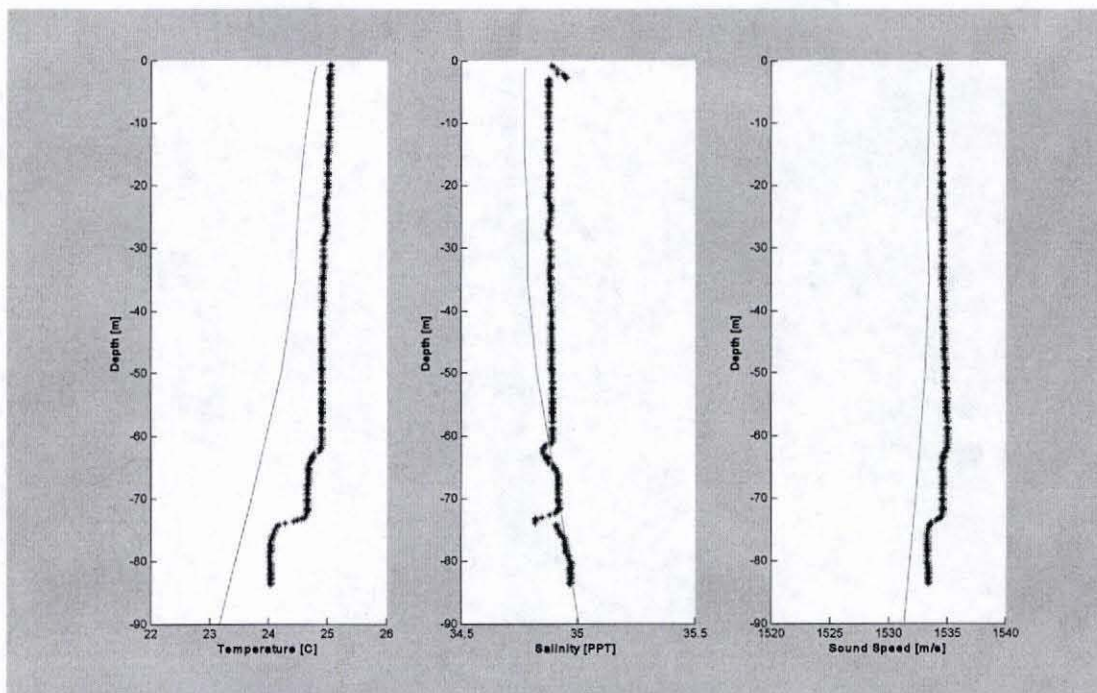


Figure 27 : Field Cast 9 Data Comparison

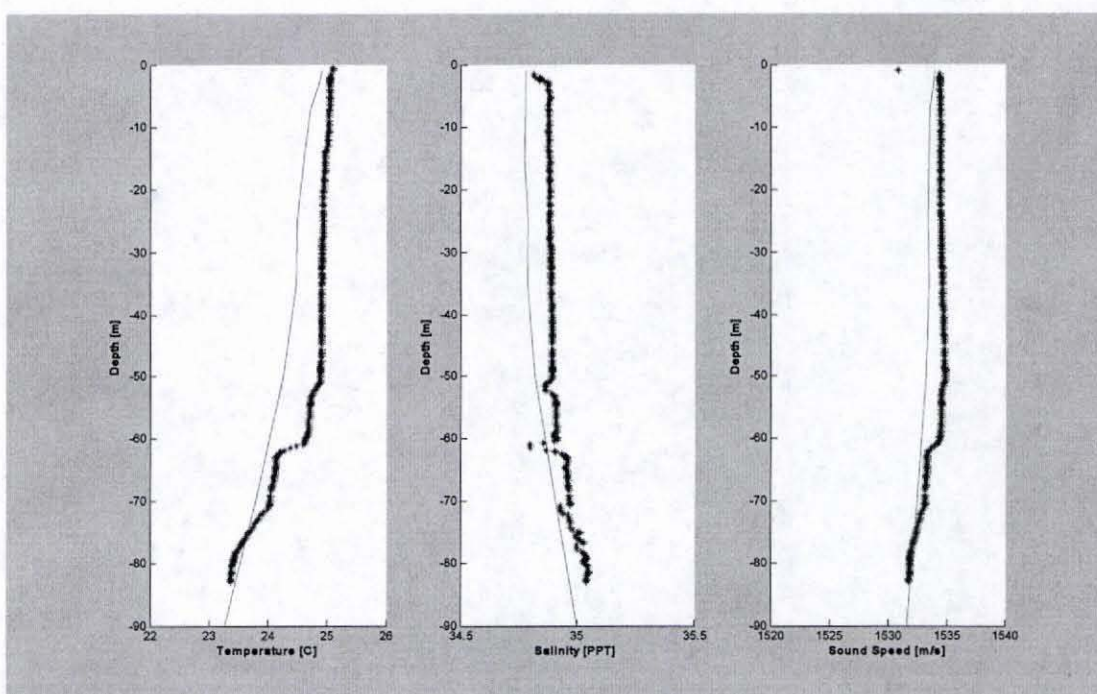


Figure 28 : Field Cast 10 Data Comparison

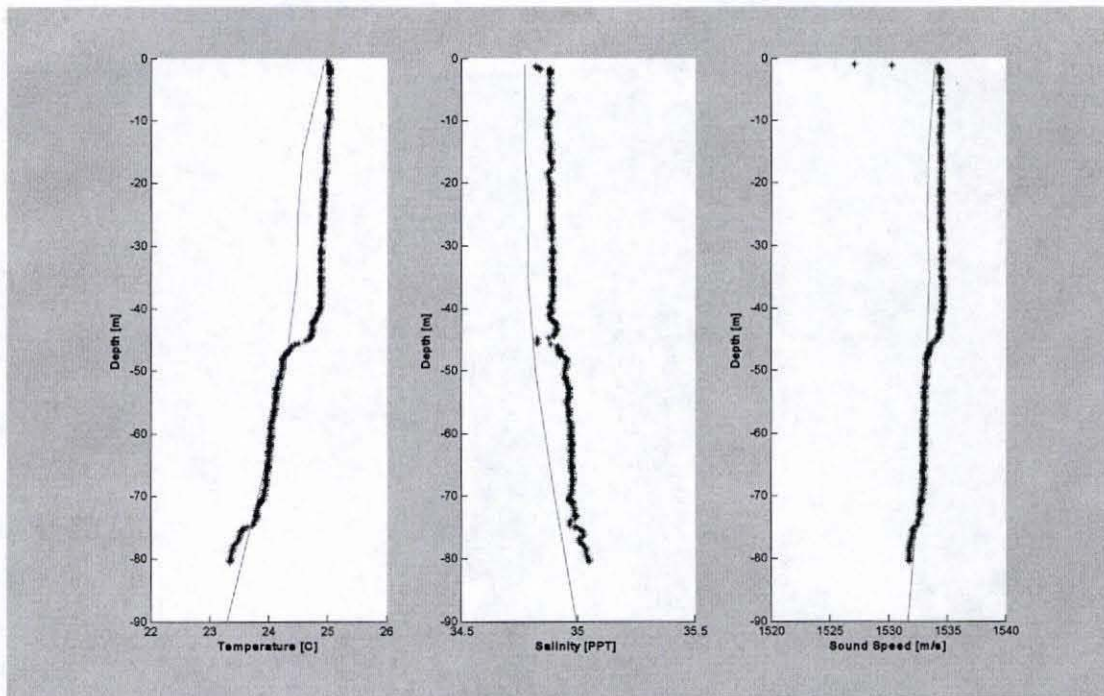


Figure 29 : Field Cast 11 Data Comparison

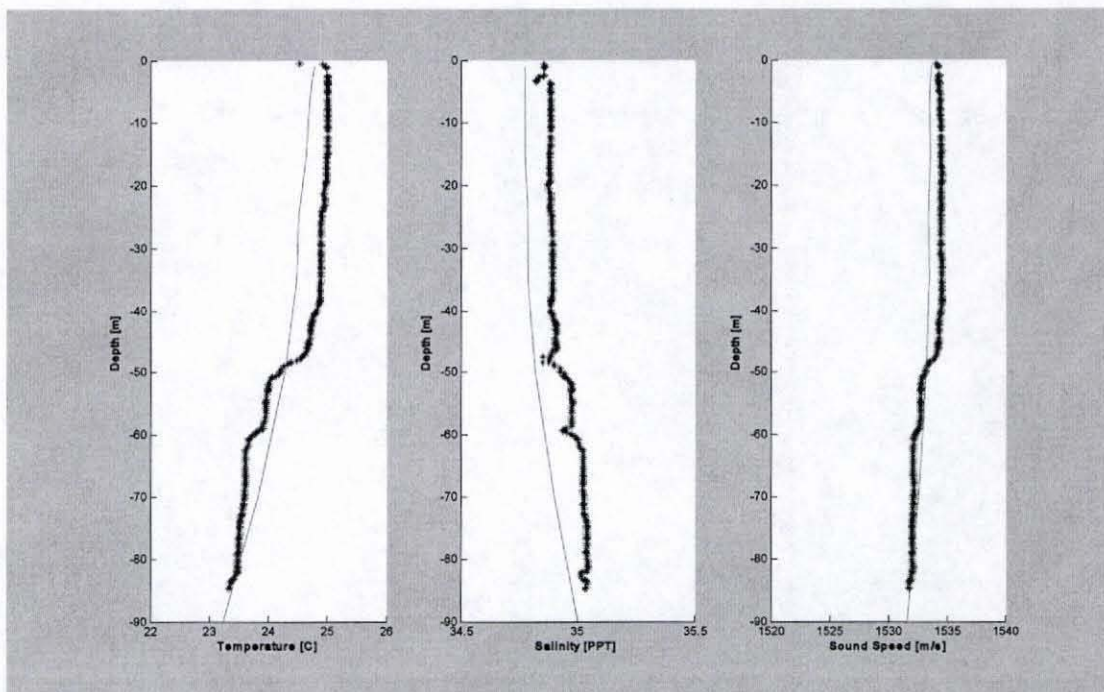


Figure 30 : Field Cast 12 Data Comparison

Appendix F: Field Cast Statistics

Field Cast	Includes Layer 1		Without Layer 1	
	Correlation Coefficient	Average Error	Correlation Coefficient	Average Error
1	0.9905	0.1798	0.9907	0.1924
2	0.9492	0.1866	0.9560	0.1930
3	0.9583	0.1731	0.9588	0.1759
4	0.9894	0.1476	0.9896	0.1487
5	0.9824	0.2428	0.9824	0.2428
6	0.9782	0.1460	0.9766	0.1552
7	0.9922	0.2529	0.9923	0.2648
8	0.9778	0.4037	0.9792	0.3985
9	0.9766	0.2286	0.9797	0.2188
10	0.9680	0.1593	0.9740	0.1616
11	0.9703	0.1642	0.9756	0.1700
12	0.9530	0.2115	0.9583	0.2220
Average	0.9738	0.2080	0.9761	0.2120

Table 9 : Temperature Statistics

Field Cast	Includes Layer 1		Without Layer 1	
	Correlation Coefficient	Average Error	Correlation Coefficient	Average Error
1	0.4138	0.1295	0.6525	0.0372
2	0.3055	0.0477	0.8199	0.0431
3	0.4643	0.0768	0.9391	0.0696
4	0.4814	0.0772	0.7140	0.0655
5	0.9079	0.0468	0.9079	0.0468
6	0.2996	1.1539	0.9716	0.0309
7	0.2514	1.8507	0.9852	0.0568
8	0.2909	2.8934	0.9363	0.0697
9	0.2358	2.8741	0.8744	0.0606
10	0.2338	4.8753	0.9911	0.0224
11	0.2602	1.4937	0.9918	0.0207
12	0.2487	2.2950	0.9446	0.0283
Average	0.3661	1.4845	0.8940	0.0460

Table 10 : Salinity Statistics

	Includes Layer 1		Without Layer 1	
Field Cast	Correlation Coefficient	Average Error	Correlation Coefficient	Average Error
1	0.9477	0.4535	0.9461	0.4836
2	-0.2002	0.4307	-0.3334	0.4336
3	0.8401	0.4019	0.8676	0.3891
4	0.9682	0.2898	0.9691	0.3006
5	0.9510	0.5593	0.9510	0.5593
6	0.5486	1.3242	0.9561	0.3628
7	0.0998	2.1873	0.9627	0.6033
8	-0.2273	3.5978	0.7409	0.9044
9	-0.1893	3.3686	0.8469	0.4637
10	-0.1988	5.3813	0.9458	0.4352
11	0.1887	1.7500	0.9412	0.4539
12	0.1056	2.6225	0.9101	0.5417
Average	0.3195	1.8639	0.8087	0.4942

Table 11 : Sound Speed Statistics

Appendix G : Tidal Current Information

Location	Latitude [N]	Longitude [E]	Depth [m]
A2	21.281	-158.11	67
A4	21.247	-158.11	505
B2	21.284	-158.02	78
B3	21.269	-158.02	250
D2	21.280	-157.89	77
D3	21.272	-157.90	249
E2	21.241	-157.81	82
E4	21.221	-157.81	496
F3	21.242	-158.06	320

Table 12 : Tidal Current Locations

Location	Major Axis [cm/s]	Minor Axis [cm/s]	Inclination [deg]	Phase [deg]
A2	1.4437 +/- 1.144	-0.9712 +/- 1.319	160.25 +/- 96.89	273.85 +/- 90.49
A4	0.2793 +/- 0.089	-0.1859 +/- 0.085	108.01 +/- 45.90	202.16 +/- 48.89
B2	1.5258 +/- 0.548	-0.7435 +/- 0.586	28.842 +/- 35.44	17.148 +/- 31.68
B3	3.2972 +/- 0.249	0.0162 +/- 0.214	58.618 +/- 3.708	246.92 +/- 4.717
D2	2.5166 +/- 0.919	0.1644 +/- 0.127	178.38 +/- 3.413	91.050 +/- 19.77
D3	3.4162 +/- 0.348	0.2881 +/- 0.279	33.255 +/- 5.138	236.59 +/- 7.113
E2	10.770 +/- 0.892	-1.3373 +/- 0.607	158.25 +/- 3.013	63.108 +/- 4.503
E4	2.0370 +/- 0.169	0.7064 +/- 0.160	153.15 +/- 4.822	12.068 +/- 5.342
F3	4.9138 +/- 0.377	-1.9131 +/- 0.391	157.49 +/- 5.594	114.36 +/- 5.761

Table 13 : Tidal Current Ellipse Information with a 95% Confidence Interval

References

- Alford, M.H., M.C. Gregg, and M.A. Merrifield (2005). Structure, Propagation and Mixing of Energetic Baroclinic Tides in Mamala Bay, Oahu, Hawaii. *Journal of Physical Oceanography*, in press.
- Blumberg, A.F. and G.L. Mellor (1987). A Description of a Three-Dimensional Coastal Ocean Circulation Model. *Three Dimensional Coastal Models, Coastal and Estuarine Sciences*, Vol. 4, Ed. N. S. Heap, 1-16.
- Blumberg, A.F., R.P. Signall, and H.L. Jenter (1993). Modeling Transport Processes in the Coastal Ocean. *Journal of Marine Environmental Engineering*, 1, 31-52.
- Blumberg, A.F. (1996). An Estuarine and Coastal Ocean Version of POM. *Proceedings of the Princeton Ocean Model Users Meeting (POM96)*, Princeton, NJ.
- Blumberg, A.F., L.A. Khan, and J.P. St. John (1999). Three-Dimensional Hydrodynamic Model of New York Harbor Region. *Journal of Hydraulic Engineering*, 125(8), 799-816.
- Blumberg, A. F., B.N. Kim, S. O'Neil, J.K. Lewis, P.J. Stein, S.D. Rajan, R.L. Schaffer, M.T. Calef, T. Curtin, S.K. Numrich, W. Smith, P. Maassel (2000). Use of Orthogonal Curvilinear Grids for the Representation of the Littoral Ocean Environment. *Proceedings of the Spring 2000 Simulation Interoperability Workshop*, Paper No. 00S-SIW-118, March 2000, Simulation Interoperability Standards Organization.

- Booij, N., R.C. Ris, and L.H. Holthuijsen (1999). A Third Generation Model for Coastal Regions, Part I: Model Description and Validation. *Journal of Geophysical Research*, 104(C4), 7649-7666.
- Brutzman, D.P. (1994). A Virtual World for an Autonomous Underwater Vehicle. PhD Dissertation, Naval Postgraduate School, Monterey, California.
- Bruzzone, Ga., Bono, R., Caccia, M., and Veruggion, G. (2001). A simulation environment for unmanned underwater vehicles development. MTS/IEEE Oceans 2001, Honolulu (USA), pp.1066-1072.
- Choi, S.K., Menor, S.A., and Yuh J. (2000). Distributed virtual environment collaborative simulator for underwater robots. IEEE/RSJ International Conference on Intelligent Robots and Systems, Takamatsu (Japan), pp. 861-866.
- Connolly, J.P., A.F. Blumberg, and J.D. Quadrini (1999). Modeling Fate of Pathogenic Organisms in Coastal Waters of Oahu, Hawaii. *Journal of Environmental Engineering*, 125(5), 398-406.
- Egbert, G.D., A.F. Bennett, and M.G.G. Foreman (1994). TOPEX/POSEIDON Tides Estimated Using a Global Inverse Tide Model. *Journal of Geophysical Research*, 99(C12), 24821-24852.
- Egbert, G.D. (1997). Tidal Data Inversion: Interpolation and Inference. *Progressive Oceanography*, 40, 53-80.
- Egbert, G.D., and S.Y. Erofeeva (2002). Efficient Inverse Modeling of Barotropic Ocean Tides. *Journal of Atmospheric Oceanic Technology*, 19(2), 183-204.

- Eich, M. L., M. A. Merrifield, and M. H. Alford (2004). Structure and Variability of Semidiurnal Internal Tides in Mamala Bay, Hawaii. *Journal of Geophysical Research*, 109(C18), 5010-5022.
- Environment Hawaii (1995). Mamala Bay Study Commission Issues Draft Report on Coastal Pollution. *Environment-Hawaii*, 6(6).
- Ezer, T. and G.L. Mellor (1997). Simulations of the Atlantic Ocean with a Free Surface Sigma Coordinate Ocean Model. *Journal of Geophysical Research*, 102(C7), 15647-15657.
- Ezer, T. (1999). Decadal Variabilities of the Upper Layers of the Subtropical North Atlantic: An Ocean Model Study. *Journal of Physical Oceanography*, 29(12), 3111-3124.
- Ezer, T. (2001). On the Response of the Atlantic Ocean to Climatic Changes in the High Latitudes: Sensitivity Studies with a Sigma-Coordinate Ocean Model. *The Oceans and Rapid Climate Change: Past, Present, and Future*, Ed. D. Seidov, B.J. Haupt, and M. Maslin. American Geophysical Union, *Geophysical Monograph*, 126, 199-215.
- Fofonoff, N.P. (1962). Physical Properties of Seawater. In *The Sea: Ideas and Observations on Progress in the Study of the Seas, Vol. 1: Physical Oceanography*, Ed. M.N. Hill, Wiley, Interscience, New York, 3-30.
- Fofonoff, P. and Millard, R.C. Jr. (1983). Algorithms for Computation of Fundamental Properties of Seawater. *Unesco Technical Papers in Marine Science*, 44, 1-53.
- Ford, A. (1999). *Modeling the Environment: An Introduction to System Dynamics Modeling of Environmental Systems*. Ed. Island Press, Washington DC.

- Fossen, T.I. (2002). Marine Control Systems: Guidance, Navigation and Control of Ships, Rigs and Underwater Vehicles. *Marine Cybernetics AS*, Trondheim.
- Fox, D.N., W.J. Teague, and C.N. Barron (2001). The Modular Ocean Data Assimilation System (MODAS). *Journal of Atmospheric and Oceanic Technology*, 19, 240-252.
- Galperin, B., L.H. Kantha, S. Hassid, and A. Rosati (1988). A Quasi-Equilibrium Turbulent Energy Model for Geophysical Flows. *Journal of Atmospheric Sciences*, 45, 55-62.
- Gerritsen, F. (1978). Beach and surf parameters in Hawaii. *Sea Grant Technical Report*. UNIH-SEAGRANT-TR-78-02.
- Hamilton, P., J. Singer, and E. Waddell (1995). Ocean Current Measurements. Report No. MB-6, Mamala Bay Study Commission, Honolulu.
- Holloway, P.E., and M.A. Merrifield (1999). Internal Tide Generation by Seamounts, Ridges, and Islands. *Journal of Geophysical Research*, 104, 25937-25951.
- HydroQual (2001). A Primer for ECOMSED. Report No. HQI-EH&S0101. HydroQual, Mahwah, NJ.
- Kanamitsu, M. (1989). Description of the NMC Global Data Assimilation and Forecast System. *Weather and Forecasting*, 4, 335-342.
- Kincaid, Ikaika (2005). Identification and Tracking of the Sand Island Sewage Outfall Plume off the Southern Shore of Oahu Using CTD Casts. MS Thesis, University of Hawaii, Department of Ocean and Resources Engineering, Honolulu, Hawaii.
- Laevastu, T., D.E. Avery, and D.C. Cox. (1964). Coastal Currents and Sewage Disposal in the Hawaiian Islands. HIG-64-1. Hawaii Institute of Geophysics, University of Hawaii, Honolulu.

- Lewis, J.K., I. Shulman, and A.F. Blumberg (1998). Assimilation of Doppler Radar Current Data into Numerical Ocean Models. *Continental Shelf Research*, 18, 541-559.
- Lewis, J.K., M.M. Merrifield, and M.L. Eich (2001). Numerical Simulations of Internal Tides Around Oahu, Hawaii. *Estuarine and Coastal Modeling: Proceedings of the Seventh International Conference*, Ed. M.L. Spaulding, *et al.*, American Society of Civil Engineers, 185-203.
- Luther, D.S. and the HOME Pls (1999). The Hawaii Ocean Mixing Experiment: Is the Abyssal Stratification Maintained by Tidalgenic Mixing?. *Proceedings of the 11th 'Aha Huliko'a Hawaiian Winter Workshop*, University of Hawaii, January 1999, 57-62.
- Martin, P. J., G. Peggion, and K. J. Yip (1998). A Comparison of Several Coastal Ocean Models. *Naval Research Laboratory*, NRL/FR/7322-97-9672, 96.
- Mellor, G.L., and T. Yamada, (1982). Development of a Turbulence Closure Model for Geophysical Fluid Problems. *Revolutionary Geophysics and Space Physics*, 20, 851-875.
- Mellor, G.L. and T. Ezer (1991). A Gulf Stream Model and an Altimetry Assimilation Scheme. *Journal of Geophysical Research*, 96, 8779-8795.
- Merrifield, M.A., and P.E. Holloway (2001). Model Estimates of M2 Internal Tide Energetics at the Hawaiian Ridge, submitted to J. Geophys. Res., 2001.
- Merrifield, M.A., P.E. Holloway, T.M. S. Johnston (2001). Internal Tide Generation at the Hawaiian Ridge. *Geophysical Research Letters*, 28, 559-562.

- Office of Naval Research (2004). The Navy Unmanned Undersea Vehicle (UUV) Master Plan. 9 November 2004.
- Podman, L. and S. Erofeeva (2004). A Barotropic Inverse Tidal Model for the Arctic Ocean. *Geophysical Research Letters*, 31(2), L02303, doi:10.1029/2003GL019003.
- Post, D.E. and L.G. Votta (2005). Computational Science Demands a New Paradigm. *Physics Today*, January 2005, 35-41.
- Pawlowicz, R., B. Beardsley, and S. Lentz (2002). Classical Tidal Harmonic Analysis Including Error Estimates in MATLAB Using T_TIDE. *Computers and Geosciences*, 28, 929-937.
- Ris, R.C. (1997). Spectral Modeling of Wind Waves in Coastal Areas. PhD Dissertation, Delft University of Technology, Department of Civil Engineering, *Communications on Hydraulic and Geotechnical Engineering*, Report No. 97-4, Delft, The Netherlands.
- Roberts, P.J.W. (1999a). Modeling Mamala Bay Outfall Plumes I: Near Field. *Journal of Hydraulic Engineering*, 125(6), 564-573.
- Roberts, P.J.W. (1999b). Modeling Mamala Bay Outfall Plumes II: Far Field. *Journal of Hydraulic Engineering*, 125(6), 574-583.
- Sea Engineering and OCEES (2005). Sand Island Ocean Outfall Lagrangian Current Monitoring. Prepared for the Department of Environmental Services of the City and County of Honolulu by Sea Engineering and OCEES of Honolulu Hawaii, July 2005, Job No. 2-29.
- Smith, W.H.F. and D.T. Sandwell (1997). Global Sea Floor Topography from Satellite Altimetry and Ship Depth Soundings. *Science*, 277, 1956-1962.

- Society of Naval Architects and Marine Engineers (SNAME) (1989). *Principles of Naval Architecture, Volume 3: Motions in Waves and Controllability*, Ed. Author, Jersey City, NJ.
- St. Denis, M. (1974). Hawaii's Floating City Development Program: The Winds, Currents and Waves at the Site of the Floating City Off Waikiki. UNIH-SEAGRANT-CR-75-01, Sea Grant College Program, University of Hawaii, Honolulu. Also Technical Report No. 1, Oceanic Institute, Waimanalo.
- Tetra Tech (2000). Ocean Circulation and Plume Dispersion Modeling Review, with Emphasis on Orange County Sanitation District's Offshore Outfall and Wastewater Plume. Prepared for Orange County Sanitation District by Tetra Tech, Inc. of Lafayette California, September 2000.
- Tolman, H.L. (2002). Validation of WaveWatch III Version 1.15 for a Global Domain, NOAA/NWS/NCEP/OMB-213.
- Torresan, M.E., M.A. Hampton, M.H. Gowen, J.H. Barber, Jr., L.L. Zink, T.E. Chase, F.L. Wong, J.T. Gann, and P. Dartnell (1995). Final Report: Acoustic Mapping of Dredged Material Disposal Sites and Deposits in Mamala Bay, Honolulu, Hawaii. U.S. Geological Survey Open-file Report 95-17.
- Vandermark, D., N. Tran, B.D. Beckley, B. Chapron, P. Gaspar (2002). Direct Estimation of Sea State Impacts on Radar Altimeter Sea Level Measurements. *Geophysical Research Letters*, 10.1029/2002GL015776.

Wang, J.J., H.M.H. Juang, K. Kodama, S. Businger, Y.L. Chen, and J. Partain (1998).

Application of the NCEP Regional Spectral Model[™] to Improve Mesoscale Weather
Forecasts in Hawaii. *Weather and Forecasting*, 13, 560-575.